Accommodation of Plate Motion in an Incipient Strike-Slip System: The Central Walker Lane

Ian K. D. Pierce[1,2] , Steven G. Wesnousky[1] , Lewis A. Owen[3] , Jayne M. Bormann[1] , Xinnan Li[4] , and Marc Caffee[5,6]

[1]Center for Neotectonic Studies and Seismological Laboratory, University of Nevada, Reno, NV, USA, [2]Department of Earth Sciences, University of Oxford, Oxford, UK, [3]Department of Marine, Earth, and Atmospheric Science, North Carolina State University, Raleigh, NC, USA, [4]Institute of Geology, China Earthquake Administration, Beijing, China, [5]Department of Physics and Astronomy, Purdue University, West Lafayette, IN, USA, [6]Department of Earth, Atmospheric and Planetary Sciences, Purdue University, West Lafayette, IN, USA

Abstract Geodesy shows that ∼7 mm/yr of dextral shear is accumulating across the Central Walker Lane in the absence of through-going strike-slip faults. To better understand how this shear is accommodated, we describe and quantify the patterns and slip rates of active faults extending between the Lake Tahoe and Walker Lake basins. Lidar data and geomorphic mapping show linear fault traces and stepping fault geometries consistent with the accommodation of dextral oblique-slip motion along the Wassuk and Smith Valley faults, whereas the Mason and Antelope valley faults are primarily dip-slip. Vertical slip rates based on cosmogenic ages in Antelope, Smith, and Mason valleys are $0.5^{+0.5}/_{-0.3}$, $0.5^{+0.7}/_{-0.4}$, and $0.04^{+0.05}/_{-0.03}$ mm/yr, respectively. A strike-slip fault in the Pine Grove Hills has a dextral slip rate of 0.3–0.8 mm/yr. The remaining unaccounted-for shear is expected to be accommodated by off-fault deformation, including block rotations, broad co-seismic warping, and complex rupture patterns. Together these faults form a left-stepping en echelon series of dextral, oblique, and normal faults that extend from south of Walker Lake to north of Lake Tahoe, similar to patterns observed in the initial stages of dextral shear laboratory models. GPS profiles spanning the entire Walker Lane are compared to these new and previously published slip rates, and show that while kinematic efficiency is ∼60% and ∼90% in the Northern and Southern Walker Lane, respectively, it is only ∼25% in the Central Walker Lane.

Plain Language Summary While most of the 2" per year of strike-slip motion between the Pacific and North America plates is accommodated along the San Andreas fault, the Walker Lane accommodates ∼20% of that motion in a ∼100 mile wide zone of faults east of the Sierra Nevada Mountains. We expect that this motion should be accommodated by strike-slip faults. We use high resolution imagery and topographic data to search for strike-slip faults in the area between Lake Tahoe, CA and Walker Lake, NV. We find some of these faults, but they do not produce sufficient earthquakes to make up the expected motion. Thus, we expect future earthquakes in this area may occur on very slow moving faults, that do not leave much lasting evidence on the landscape- similar to the 2019 Ridgecrest earthquakes. In the future this zone of faults may accommodate more slip, forming a continuous fault similar to the San Andreas.

1. Introduction

As geodesy is increasingly used to inform seismic hazards (e.g., Field et al., 1999; Petersen et al., 2014; Riguzzi et al., 2012; Rollins & Avouac, 2019; Wesnousky et al., 2012), it is important to understand how geodetic observations relate to paleoseismic evidence preserved in the geologic record. In the Central Walker Lane, between the latitudes of Lake Tahoe and Walker Lake (Figure 1), GPS measurements indicate that the Walker Lane accommodates ∼7 mm/yr of northwest directed dextral shear (Bormann et al., 2016; Hammond & Thatcher, 2005, 2007; Hammond et al., 2011; Thatcher et al., 1999). Over half of this total ∼7 mm/yr of shear cannot be accounted for by summing the geologic slip rates of the few known strike-slip faults in this region that is otherwise composed of a series of normal fault bound basins (Wesnousky et al., 2012). The motivations of this study are as follows: (1) to determine the reasons for the discrepancy between geologic and geodetic rates, (2) to describe how shear is accommodated across this part of the Walker Lane, and (3) to propose a model that explains the discrepancy in the context of a maturing, continental-scale shear zone.
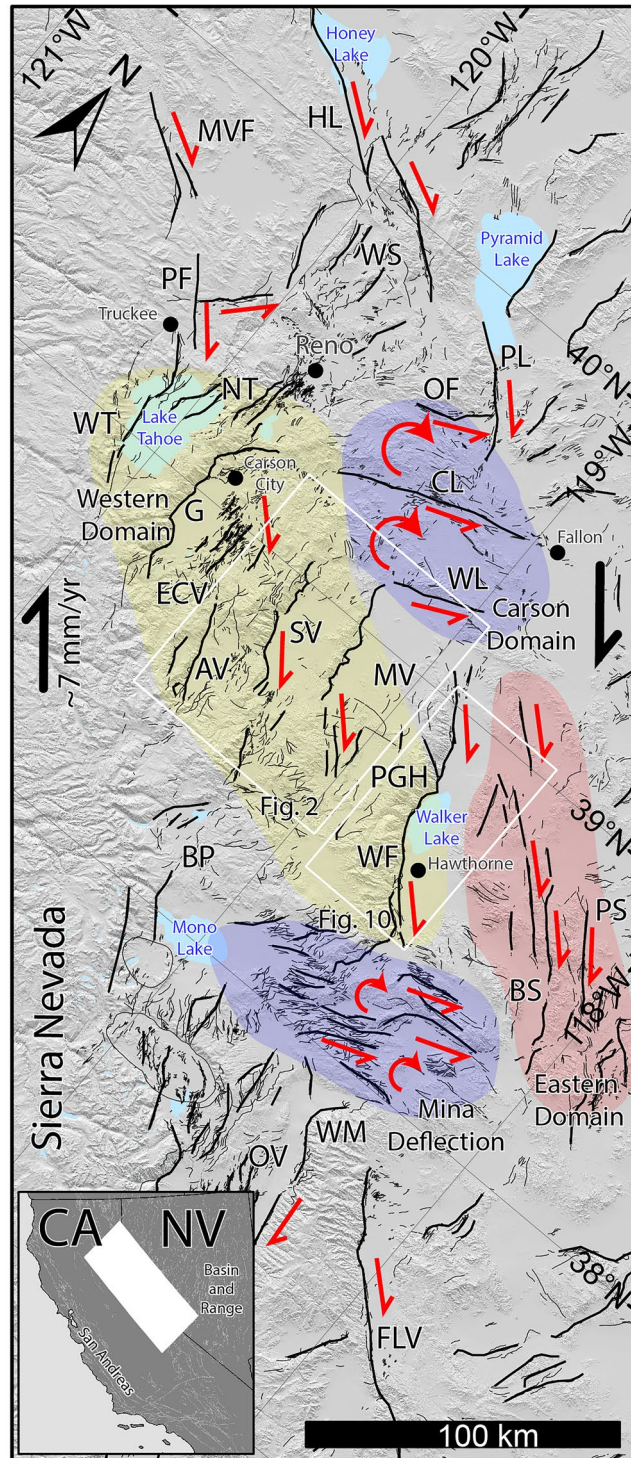
Figure 1. Overview map of the Walker Lane. Extent of Figures 2 and 10 are indicated by white boxes. Major faults are thicker while thin faults are from USGS Quaternary fault and fold database (USGS, 2020). The Central Walker Lane can be divided into the sinistral Carson domain and Mina Deflection (purple), western domain (yellow), and dextral eastern domain (pink). Major faults: MVF, Mohawk Valley; HL, Honey Lake; WS, Warm Springs; PF, Polaris; PL, Pyramid Lake; OF, Olinghouse; WT, West Tahoe; NT, North Tahoe (from west to east: Stateline, Incline Village, Little Valley, Washoe Lake), G, Genoa; ECV, East Carson Valley; AV, Antelope Valley; SV, Smith Valley; CL, Carson Lineament; WL, Wabuska Lineament; MV, Mason Valley; PGH, Pine Grove Hills; BP, Bridgeport Valley; WF, Wassuk Fault; BS, Benton Springs; PS, Petrified Springs; OV, Owens Valley; WM, White Mountains; FLV, Death Valley-Fish Lake Valley.

To achieve these goals, we use high-resolution topographic data and imagery to search for evidence of previously unreported strike-slip faulting and to map the tectonic geomorphology of a part of the Walker Lake basin, the Pine Grove Hills, and Antelope, Mason, and Smith valleys. We present observations of northwest oriented dextral motion along both previously mapped and newly mapped sections of faults throughout the study region. We calculate rates of slip for each of the major range bounding faults in these basins using cosmogenic nuclide boulder and sediment samples from faulted alluvial fan surfaces. We then present GPS profiles of transects across the entire Walker Lane. These observations form the basis of discussions focused on resolving geologic and geodetic discrepancies and the structural evolution of shear zones.

2. Regional Context

The Walker Lane Belt (Stewart, 1988) is a ~500-km-long by 100-km-wide northwest trending zone of discontinuous active faults and disrupted topography that sits between the Sierra Nevada to the west and the Basin and Range to the east (Figure 1). Roughly 20% of the ~50 mm/yr of dextral shear between the Pacific and North American plates (Bennett et al., 2003; Dixon et al., 2000; Thatcher et al., 1999; Unruh et al., 2003) is accommodated by the normal and strike-slip faults that compose the Walker Lane. The Walker Lane is well defined geodetically by a zone of ~9 mm/yr of northwest directed dextral shear at the latitude of Owens Valley, decreasing to ~7 mm/yr at the latitude of Reno, NV (e.g., Bormann et al., 2016; Hammond et al., 2011; Wesnousky et al., 2012). Cumulative dextral shear also decreases from ~110 km across the southern part (e.g., Guest et al., 2007) to 20–30 km across the northern part (Faulds et al., 2005). These decreases and the broad, discontinuous nature of faulting in the Walker Lane have been cited as evidence of the youthful expression of an incipient transform boundary (e.g., Faulds & Henry, 2008; Faulds et al., 2005).

The Northern Walker Lane encompasses the northwest-striking dextral strike-slip Pyramid Lake (Angster et al., 2016; Briggs, 2004), Warm Springs (Chupik, 2019; R. Gold et al., 2013), Honey Lake (R. D. Gold et al., 2017), Polaris (Hunter et al., 2011), and Mohawk Valley (R. D. Gold et al., 2014) faults (Figure 1). The Southern Walker Lane is composed of predominantly northwest-striking dextral and normal faults, including the Owens Valley (Beanland & Clark, 1994; Haddon et al., 2016; Kirby et al., 2008; Lee et al., 2001), Fish Lake Valley-Furnace Creek-Death Valley (Frankel et al., 2007, 2011; Ganev et al., 2010), and White Mountains (Kirby et al., 2006; Stockli et al., 2003) faults. The Central Walker Lane interrupts the overall northwest structural grain of the Walker Lane with a series of north-striking range-bounding normal faults, transverse sinistral faults, and northwest-striking dextral faults.

The Central Walker Lane is here further subdivided into four domains based on orientations and kinematics of faults (Figure 1). The northerly Carson domain (e.g., P. H. Cashman & Fontaine, 2000; Li et al., 2017; Wesnousky, 2005) is composed of the northeast-striking, sinistral Olinghouse fault (Briggs & Wesnousky, 2005), and the Carson and Wabuska lineaments (Li et al., 2017). This domain has accommodated >50° of clockwise vertical axis rotation since the Miocene (Carlson, 2017; P. H. Cashman & Fontaine, 2000). The eastern domain, modified here after the Walker Lake block of Stewart (1988), includes the northwest-striking dextral strike-slip Benton Springs, Indian Head, Gumdrop, and Petrified Springs faults (Angster et al., 2019; Wesnousky, 2005). Together, these closely spaced faults accommodate ~4 mm/yr of dextral shear (Angster et al., 2019). The southerly Mina Deflection (e.g., Wesnousky, 2005) is composed of east-west-striking sinistral faults and forms a large right step between the dextral faults of the Southern Walker Lane and the eastern domain of the Central Walker Lane.

The western domain of the Central Walker Lane encompasses the basins and their north-striking range-bounding faults that are the focus of this paper, including the Lake Tahoe (Kent et al., 2005; Maloney et al., 2013; Pierce et al., 2017) and Walker Lake (Bormann et al., 2012; Dong et al., 2014; B. Surpless & Kroeger, 2015) basins, and Carson (dePolo & Sawyer, 2005; Ramelli et al., 1999), Smith (Wesnousky & Caffee, 2011), Mason, and Antelope (Sarmiento et al., 2011) valleys (Figure 2). Dong et al. (2014) report 1 mm/yr of dextral slip near the Wassuk rangefront, but there are no other reported rates of dextral oblique- or strike-slip faults in the western or Carson domains to accommodate the ~4 mm/yr of dextral shear measured west of the Wassuk Range. GPS transects show that the observed shear is evenly spaced across the Central Walker Lane, and is not isolated to the faults of the eastern part (e.g., Bormann et al., 2016).
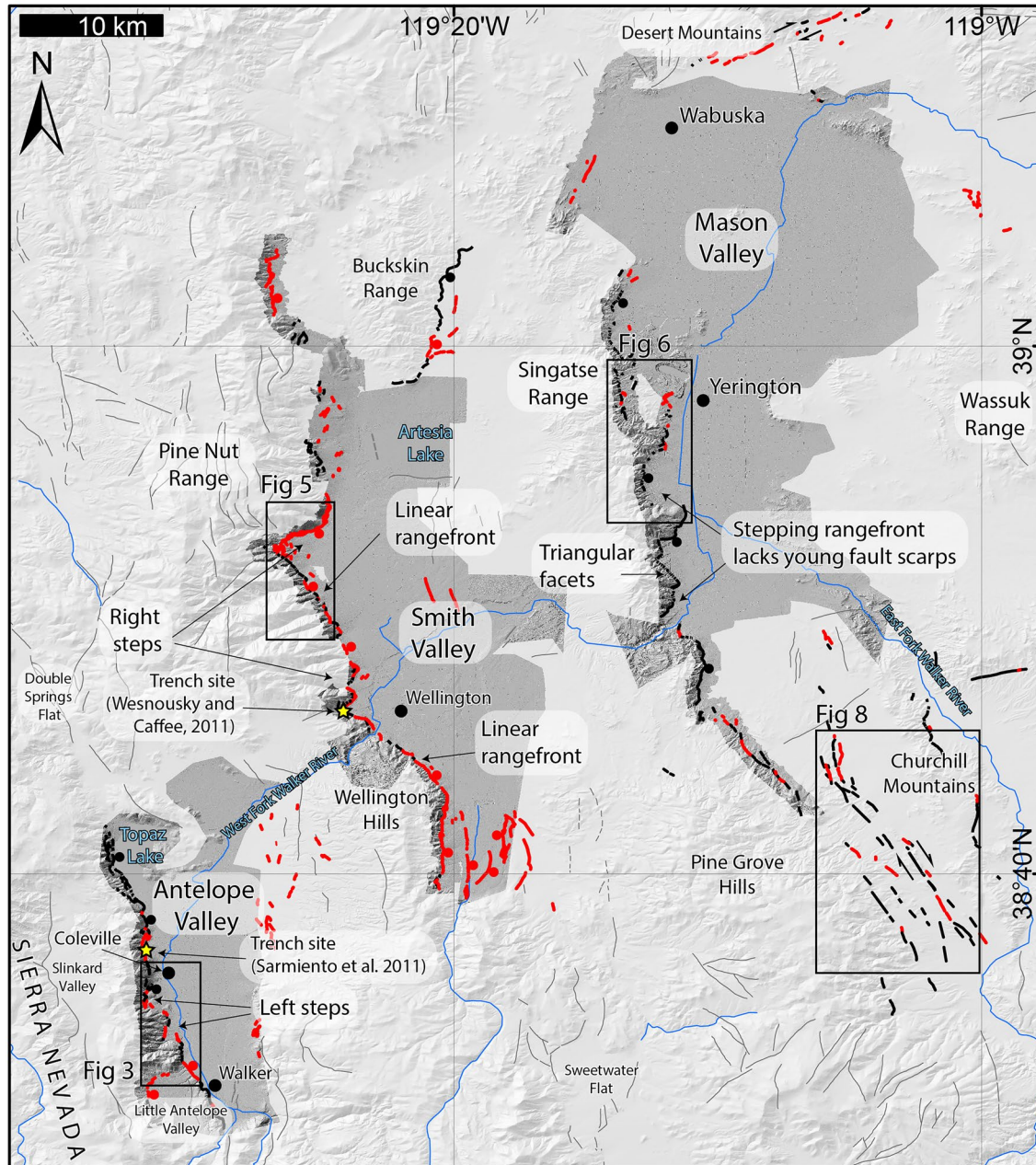
Figure 2. Overview of study area. Dark gray hillshades indicate extent of lidar data. Red lines are faults mapped in this study and observed cutting alluvial deposits, while bold black lines are bedrock-alluvial active fault contacts. Thin black lines are faults from USGS Quaternary fault and fold database (USGS, 2020). Black boxes indicate the extent of Figures 3, 5, 6, and 8.

To explain the discrepancy between geologic and geodetic measurements, Wesnousky et al. (2012) propose that in the absence of dextral faults, range scale clockwise block rotations and asymmetric, northward-opening basins accommodate the observed geodetic shear across the western domain of the Central Walker Lane. However, GPS driven block models (e.g., Bormann et al., 2016) show that dextral shear in the western domain cannot be accommodated through normal faulting and block rotations alone, suggesting that some component of dextral oblique slip is needed to accommodate shear in this region. Thus, unrecognized oblique-slip faulting in the western domain may play a larger role in accommodating Walker Lane shear than previously thought.

3. Methods

3.1. Quaternary Mapping

Descriptions of faulting characteristics along each of the faults and lineaments are derived from the analysis of large-scale (~1:12,000) low-sun-angle black and white aerial photographs (Center for Neotectonic Studies library), Google Earth imagery, structure-from-motion models, and lidar data. Lidar data were compiled from three existing data sets acquired by the USGS (2009 Walker Lake Lidar), Desert Research Institute (2010 Walker River Lidar), and National Wildlife Service (2006 Walker River Lidar) and ~334 km^2 of new data acquired in 2015 for this study through the National Center for Airborne Laser Mapping (2015 Walker Fault System NV Lidar available on OpenTopography.org). Metadata for the previously existing data sets are available at the US Interagency Elevation Inventory (coast.noaa.gov/inventory). For each basin, the lidar data sets are merged into a seamless data set with contour, hill-shade, and slope-shade maps derived for geomorphic analysis. A structure-from-motion elevation model of part of the Pine Grove Hills fault was generated using Agisoft Photoscan Pro with images collected using a DJI Phantom 3+ quadcopter. Images are georeferenced from sites located in a target region using a Trimble R10 dGPS unit, resulting in a ~25 cm/pixel gridded elevation model, that is available on OpenTopography.org. All faults mapped in this study are included in part in the Quaternary fault and fold database (USGS, 2020) and other prior regional geologic maps (e.g., Dohrenwend, 1982), but are presented here in greater detail as the mapping in this study is based on high-resolution topographic data and imagery, and not from prior geologic maps.

We present generalized surficial maps based on interpretations of lidar data and satellite imagery for the Pine Grove Hills and Mason, Smith, and Antelope valleys (e.g., Plate 1 (supporting information) and Figures 3, 5, 6, and 8). Maps are constructed following the relative geomorphic age methods outlined in Bull (1991) as used in other studies in this region (e.g., Bell et al., 2004; Koehler & Wesnousky, 2011; Li et al., 2017; Sarmiento et al., 2011; Wesnousky, 2005; Wesnousky & Caffee, 2011). All specific sites described in the following sections were field verified, but not every alluvial fan surface mapped in Plate 1 was visited in the field. Deposits are divided into units based on relative age and type of geomorphic landform/sediment: fluvial (Qfl), basin fill (Qbf), playa/lacustrine (Qp), aeolian (Qd), and four alluvial fan units (Qa-active, Qy-young, Qi-intermediate, and Qo-old). Land obscured by anthropogenic activity (anth) and undivided bedrock (bx) are also mapped. Fault traces in Figures 2, 3, 5, 6, 8, and 10 are divided as either fault scarps that are clearly expressed in Quaternary deposits (red lines) or as inferred faults and/or fault contacts between Quaternary deposits and bedrock (black lines). Alluvial fan units are divided by relative age primarily using height above modern stream grade, amount of dissection, height of fault scarp (if present), and textural differences in imagery and lidar data. Age estimates for alluvial fan units are either from cosmogenic ages presented in the following sections, or based on relative age relationships to the Qi alluvial fan surfaces, which are the youngest fans that are modified by shoreline processes when near the highstand of Lake Lahontan (Adams & Wesnousky, 1998; Reheis, 1999).

Old alluvial fan units (Qo) are the highest alluvial fan units and are often incised >10 m with well-rounded interfluves. The surfaces have soils with clay-rich Bt horizons and well-developed carbonate (Birkeland, 1984). Following others mapping in the region (e.g., Wesnousky, 2005), the Qo alluvial fans are considered to be mid-to late Pleistocene in age. Intermediate alluvial fans (Qi) sit at elevations below Qo deposits in respective map areas, are moderately incised with well-developed drainage networks, and are modified by shoreline deposits when near the highstand of Lake Lahontan. Thus, Qi alluvial fans are considered late Pleistocene in age. Qy alluvial fans are low lying, and have smooth surfaces in lidar, and a dark tone in imagery. Qy alluvial fans are Holocene and latest Pleistocene. Qa alluvial fans represent active washes and alluvial fans, and are differentiated from Qy alluvial fans by lighter tone on imagery and well-defined channel morphology. Where faults are present, Qy alluvial fans are sometimes differentiated from Qa alluvial fans by fault scarps that do not cut the younger Qa alluvial fans. Most mapped Quaternary alluvial fan units presented here match these descriptions; we note any site specific variations in the following sections.

3.2. Geochronology

Alluvial fan ages are based on measurements of cosmogenic ^{10}Be and ^{36}Cl concentrations of surface boulders and a single ^{10}Be depth profile (e.g., Frankel et al., 2007; Kirby et al., 2006, 2008; Owen et al., 2011;

Phillips et al., 1990). Over time, cosmic rays produce nuclides in minerals on Earth's surface, and by modeling the rate at which these nuclides accumulate we estimate the exposure age of surficial materials (Gosse & Phillips, 2001). Considerable variance in samples from alluvial fans results largely from inheritance, that is, exposure of materials prior to their final deposition (e.g., Frankel et al., 2007; Owen et al., 2011). We sampled at least six boulders per surface to help account for this variance.

Both [10]Be and [36]Cl concentrations were measured at the PRIME lab at Purdue. All [10]Be samples were processed in the Geochronology Laboratories at the University of Cincinnati following the methods of Kohl and Nishiizumi (1992). The [36]Cl samples were processed and analyzed at the PRIME lab. Detailed descriptions of sample preparation and analysis are in the supporting information.

Boulder sampling focused on the largest boulders (∼50–150-cm-diameter) from alluvial fan surfaces. Approximately 500 g samples were taken from the upper 2–5 cm of each of these boulders. Photographs of each of the sampled boulders are provided in the supporting information. [10]Be concentrations and laboratory data are listed in Table S1. The [10]Be boulder exposure ages were calculated using the Cosmic Ray Exposure Program (CREp) of Martin et al. (2017) and are listed in Table 1. The calculator requires input describing the geographic coordinates and elevation of the samples, local shielding of the sample, density of the sample, and estimation of the boulder erosion rates resulting from processes such as boulder grussification and spalling (Gosse & Phillips, 2001). These values are listed for each sample in Table S1. All the ages are minimum ages since we assume no erosion, however the rate of erosion must be low as there is a sample with an age >450 ka (Owen et al., 2011). We do not see evidence of a systematic boulder height-age relationship that could be a result of erosion (e.g., Behr et al., 2010; Blard et al., 2007; Garvin et al., 2005; B. Surpless & Kroeger, 2015). The age estimates are also dependent on the assumption of particular scaling models designed to estimate the long-term production rate of cosmogenic [10]Be. The [10]Be ages in Table 1 use a production rate of 4.05 ± 0.30 at/g SiO_2/yr determined at Twin Lakes, which is located at a higher elevation than the fan surfaces here, but is within 100 km of all study sites (Balco et al., 2008; Borchers et al., 2016; Nishiizumi et al., 1989), the ERA40 atmosphere model of Uppala et al. (2005), the Lifton-VDM2016 geomagnetic database (N. Lifton, 2016), and the LSD scaling scheme (N. Lifton et al., 2014). Ages were also calculated using the time-dependent scaling model of Lal (1991) and Stone (2000), and these results are listed in Table S1. The [36]Cl boulder ages are calculated using the CRONUS calculator for [36]Cl, and are listed in Table 1, with laboratory details in Table S2.

To determine the age of a fan surface in Mason Valley using a cosmogenic depth profile, a ∼2-m-deep profile was excavated and the exposed sediment was sampled at 20, 45, 105, and 160 cm depths for [10]Be analysis. The resulting [10]Be concentrations as a function of depth were modeled using the Hidy et al. (2010) MATLAB code, which uses a Monte Carlo simulation to find the best fit of the data and resulting surface age. As soil descriptions are critical to correctly interpreting results of cosmogenic ages (e.g., Angster et al., 2019), the soil exposed in the profile was described following Birkeland (1984) and soil textural grain size was analyzed by A&L Great Lakes Laboratories, Inc.

3.3. Vertical Separation Measurements

Both normal fault slip rates and fault slip distributions require measurements of vertical separation. Fault scarp vertical separations are determined by extracting topographic profiles from lidar data. Topographic profiles are extracted approximately orthogonal to fault scarps where both hanging and footwall surfaces are similar in age and show minimal to no modification by geomorphic and anthropogenic processes unrelated to faulting (e.g., road cuts, younger alluvial fan deposition, or fluvial modification). Profiles are analyzed using a python code written for this study (see supporting information) that fits linear regressions to points selected by the user that are representative of the hanging wall, foot wall, and fault scarp surfaces (example profile in Figure 3d). To standardize measurement where hanging wall and foot wall surfaces are not parallel, the apparent vertical separation between the two surfaces is measured at the horizontal midpoint of the intersections between the regressions of the fault scarp and each of the hanging and foot walls (modified after Caskey, 1995; Rood et al., 2011).

Table 1
Geochronology

| Method | Sample name | Location | | Elevation above sea level | Age | 1σ error |
| | | Latitude | Longitude | | | |
		(°N)	(°W)	(m)	(ka)	(ka)
Mason Valley	Upper Yerington Fan					
^{10}Be Boulder	MVS1	38.9669	119.2012		1,424	37.2
^{10}Be Boulder	MVS2	38.9661	119.2019		1,430	6.6
^{10}Be Boulder	MVS3	38.9660	119.2034	857	183.5	13.5
^{10}Be Boulder	MVS4	38.9653	119.2028	1,431	90.5	6.9
^{10}Be depth profile	M1-Pit	38.9669	119.2012	1,425	173.1	$^{38.7}/_{-32.5}$
Smith Valley	Artesia Fan—intermediate surface					
^{10}Be Boulder	SF1	38.8908	119.4158	1,494	30.2	2.6
^{10}Be Boulder	SF2	38.8909	119.4163	1,497	19.3	1.6
^{10}Be Boulder	SF3	38.8903	119.4158	1,491	40.4	2.8
	Artesia Fan—intermediate surface (Wesnousky & Caffee, 2011)					
^{10}Be Boulder	CWL-2	38.8907	119.4150	1,480	32.5	3.0
^{10}Be Boulder	CWL-3	38.8907	119.4148	1,470	40.7	3.7
^{10}Be Boulder	CWL-4	38.8907	119.4148	1,480	69.9	6.3
	Artesia Fan—upper younger surface					
^{10}Be Boulder	SF4	38.8892	119.4164	1,494	21.3	2.0
^{10}Be Boulder	SF5	38.8892	119.4165	1,494	12.1	1.7
^{10}Be Boulder	SF6	38.8893	119.4171	1,500	34.7	2.9
	Artesia Fan—lower younger surface					
^{10}Be Boulder	SF8	38.8892	119.4149	1,468	27.4	2.6
^{10}Be Boulder	SF9	38.8892	119.4148	1,472	26.6	3.0
^{10}Be Boulder	SF10	38.8894	119.4145	1,458	13.4	2.1
^{10}Be Boulder	SF11	38.8888	119.4142	1,450	10.3	1.3
Antelope Valley	Walker Fan					
^{36}Cl Boulder	CWL-5	38.54039	119.5023	1,654	58.0	6.1
^{36}Cl Boulder	CWL-6	38.54071	119.5025	1,650	111.0	13.0
^{36}Cl Boulder	CWL-7	38.54069	119.5024	1,649	59.0	8.1
^{36}Cl Boulder	CWL-8	38.54164	119.5049	1,657	63.2	6.6
^{36}Cl Boulder	CWL-9	38.54169	119.5048	1,659	50.3	5.8
^{36}Cl Boulder	CWL-10	38.54208	119.5043	1,654	33.3	3.9

3.4. Slip Rate Calculations

Vertical slip rates of faults are determined by dividing the probability distribution of the vertical displacement of the fault by the distribution of ages of the displaced surface using the MATLAB code of Zechar and Frankel (2009). Resulting plots are in Figure 4. In this method, the probability distribution of the age of a surface is the sum of the probability distributions of each of the samples from a single surface. The uncertainty of the vertical separation is assumed to be normally distributed, described by the mean and standard deviation of the vertical separation determined from 3 to 5 profiles extracted perpendicular to a fault scarp in a deposit of a single age. A normal distribution is used to better estimate the average fault offset from a number of measurements of fault scarps, modified unknown amounts by erosion on the hanging wall, deposition on the footwall, and the natural variability of the earthquake displacement along fault

strike. Downdip and extensional components of slip are determined using an assumption of 55° ± 10° dipping normal fault geometries, based on gravity data, seismic reflection profiles, and the steep rangefronts throughout the study region (e.g., Cashman et al., 2009; Surpless & Kroeger, 2015). Strike-slip rates are calculated by dividing the lateral displacement by the age of the surface, and assuming a vertically dipping fault geometry. Resulting slip rates are listed in Table 2.

3.5. GPS Velocities

The Walker Lane GPS velocities presented here are from the Nevada Geodetic Laboratory MIDAS velocity solution (Blewitt et al., 2016, 2018, accessible at http://geodesy.unr.edu/velocities/). We include velocities for all GPS stations with time series longer than 2.5 years from the semicontinuous MAGNET network operated by the Nevada Geodetic Laboratory (Blewitt et al., 2009) and neighboring continuous GPS stations. The velocities are calculated using position data collected through August 2019, presented in the NA12 reference frame (Blewitt et al., 2013), and corrected for the postseismic effects of historic ruptures in and surrounding the Walker Lane.

The MIDAS algorithm is a median trend estimator that mitigates both seasonality and step discontinuities in the times series (Blewitt et al., 2016). The resulting velocities are insensitive to the coseismic and postseismic effects of earthquakes that occurred after the midpoint of the time series (Blewitt et al., 2016), such as the July 2019 Ridgecrest, CA M_w 6.4 and 7.1 sequence, but must be corrected for the postseismic effects of earthquakes that occurred prior to the middle of time series, such as the historic surface rupturing earthquakes in Central Nevada Seismic Belt and the 1993 Landers M_w 7.3, and 1999 Hector Mine M_w 7.0 events. We apply the viscoelastic postseismic relaxation correction from Bormann et al. (2013) that was developed using the method of Hammond et al. (2010) and the preferred western Basin and Range crustal and upper mantle viscosity model of Hammond et al. (2009). The observed and postseismic-corrected velocities are plotted GPS profiles in Figure 12 and are available in Table S4 (Pierce et al., 2021). The postseismic-corrected velocities are shown in map view in Figure S1.

4. The Basins

The western domain of the Central Walker Lane is composed of the Lake Tahoe, Carson Valley, Antelope Valley, Smith Valley, Mason Valley, and Walker Lake basins. Along the western margins of each of these basins is a subparallel north-striking/east-dipping active range-bounding fault dividing a mountain range to the west from a half-graben holding the basin to the east (Figure 2). The north-strike of these mountain ranges contrasts sharply with the northeast-strike of those of the Basin and Range to the east of this region, and the continuous high topography of the Sierra Nevada to the west. These range-bounding faults are ~20–100 km long and together they form a rough left stepping en echelon pattern.

4.1. Antelope Valley

4.1.1. Geomorphic Expression of Active Faulting

The Antelope Valley rangefront is steep, rising 800 m above the valley floor, with prominent triangular facets and frequent scarps in alluvial deposits. The range-bounding fault follows an overall northwest trace for ~23 km, and consists of <5 km long, north-striking, left-stepping fault sections (Figure 2). Fault scarps range in height from ~1 to 3 m up to >20 m and are present at the mouths of most drainages in Qy, Qi, and Qo deposits (Figure 3). Nowhere along the rangefront did we find evidence of lateral displacements. Sarmiento et al. (2011) excavated a paleoseismic trench near Coleville across the range bounding fault. This trench revealed evidence of two normal fault earthquakes, occurring at 1,350 and before 6,250 cal yr BP, with dip-slip displacements of 3.6 and 3.1 m for each event, respectively.

The east side of Antelope Valley contains a series of faulted alluvial surfaces that extend westward from the crest of the Wellington Hills (Figure 2). The alluvial surfaces in the eastern part of the valley are incised by numerous small drainages and are mapped here as Qi and Qo (Plate 1). Google Earth imagery shows a series of
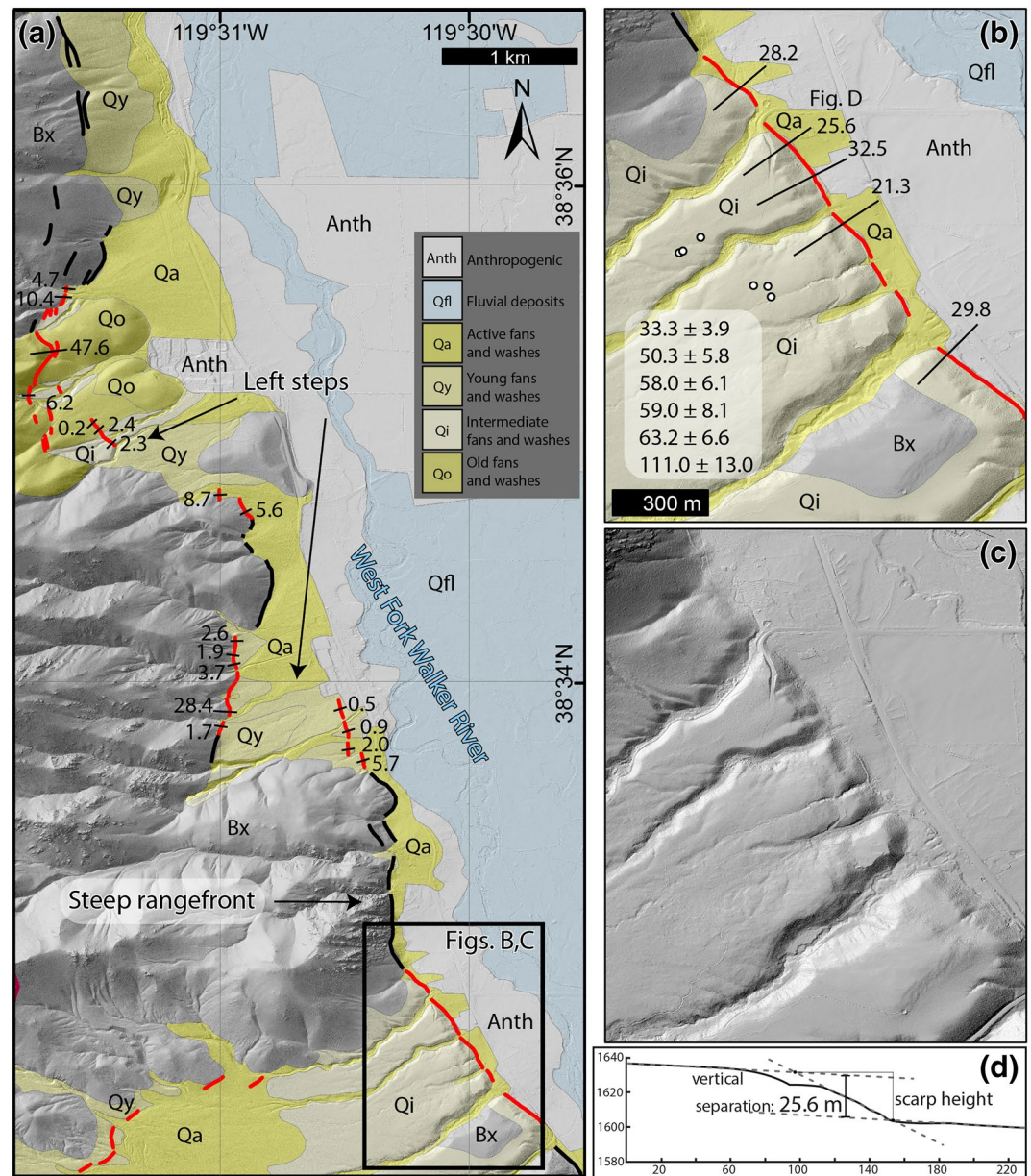
Figure 3. Section of Antelope Valley rangefront showing (a) left-stepping pattern and (b) location of Walker slip rate site. Black faults are bedrock-alluvial fault contacts. Red faults are fault scarps in alluvial deposits. Straight black lines are scarp profiles and values are scarp heights in (m). (b) Walker slip rate site interpreted and (c) bare lidar hillshade. Scarp profiles (black lines), heights (in m), and ages (ka) of boulder samples (white dots) are shown in (b). Example of profile and method used to find vertical separation in (d). Location of profile in (b).

short, discontinuous north- and northwest-trending fault scarps cutting these surfaces (Figure 2). As in the eastern part of Carson Valley (e.g., P. Cashman et al., 2009), many of the fault scarps here are uphill (east) facing.

4.1.2. Fault Slip Rate

A large uplifted alluvial fan terrace is present just northwest of the town of Walker (Figure 2). Five profiles measured across different parts of the fault scarp at this site (Figure 3c) have vertical separations ranging from 21.3 to 32.5 m, with a mean value of 27.5 ± 4.3 m. The surface here forms a ∼1-m-thick alluvial cap containing numerous boulders on a bedrock pediment surface that is incised over 20 m by drainages (Fig-

ure 3c). The faulted surface exhibits a bench of slightly lower elevation adjacent to the fault. The surface of this bench contains a thin scattered rounded cobble deposit that was likely deposited by the Walker River. Not only does the scarp itself appear to be modified by the Walker River, but also the hanging wall surface is buried by younger alluvial fan activity and fluvial deposition from the nearby Walker River, and thus this measured vertical separation is a minimum. Boulders on the Qi surface here are mostly volcanic rocks sourced from the nearby Sierra Nevada. Here, we collected six boulder samples for ^{36}Cl cosmogenic analysis (Table 1). Resulting ages range from ~33 to 111 ka (mean age of 62.4 ± 23.8 ka) (Figure 3c). Dividing the average vertical separation with this age distribution results in a vertical separation rate of 0.5 $^{+0.5}/_{-0.3}$ mm/yr (Figure 4). Based on an assumed 55° ± 10° dip, the downdip slip rate here is 0.6 $^{+0.6}/_{-0.4}$ mm/yr, encompassing the 0.7 mm/yr estimate that Sarmiento et al. (2011) made based on the displacement measured in
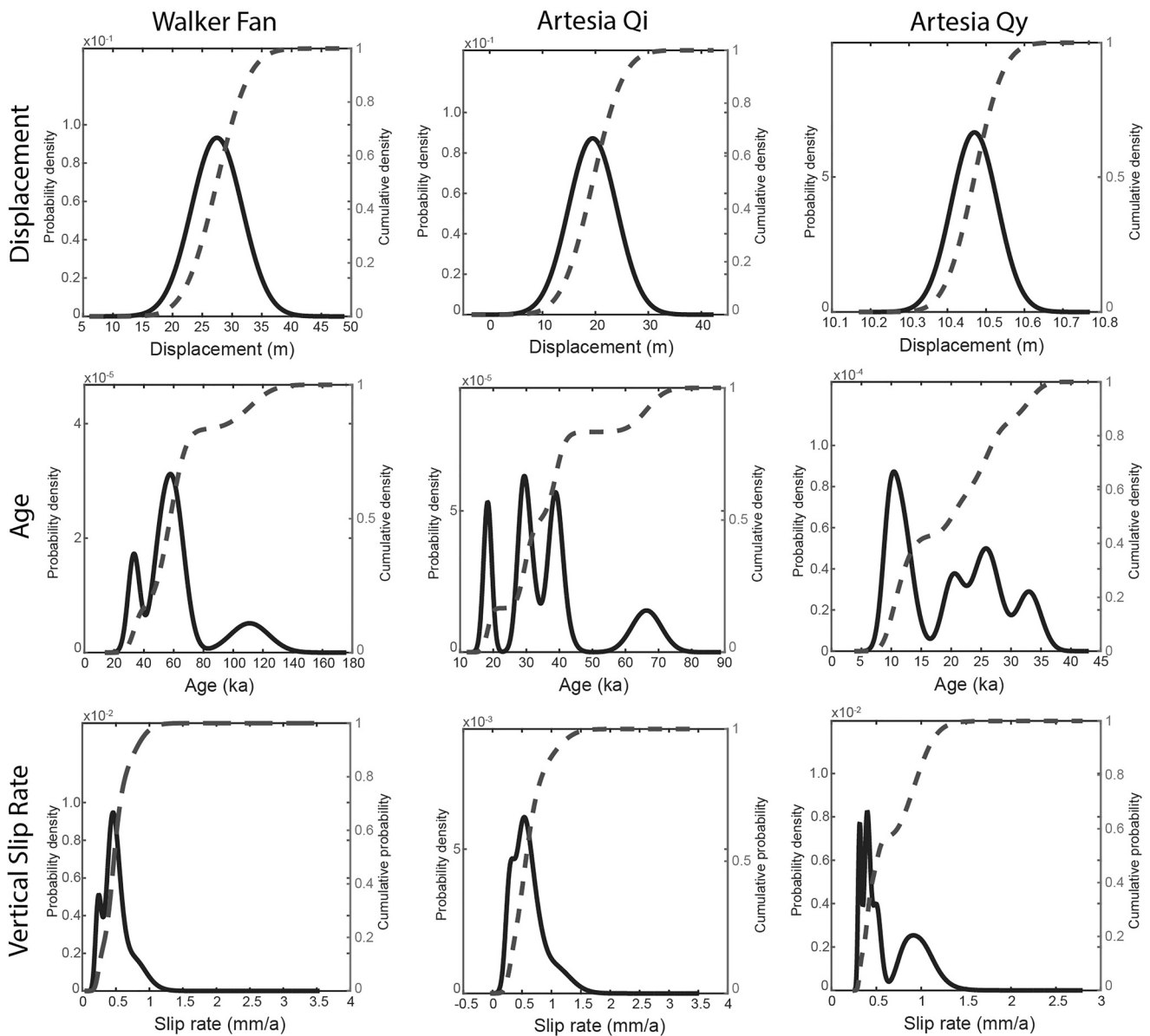

Figure 4. Displacement, age, and vertical slip rate probability distributions for the Antelope Valley and Smith Valley range bounding faults. For each plot, probability densities are the solid lines (left axis), while cumulative probabilities are the dashed lines (right axis). Plots made from code of Zechar and Frankel (2009).

their trench and the interevent time. Using the same dip results in an extension rate of 0.4 $^{+0.4}/_{-0.2}$ mm/yr (Table 2).

4.2. Smith Valley

4.2.1. Geomorphic Expression of Active Faulting

As in Antelope Valley, the Smith Valley rangefront is also steep, rising >1,400 m above the valley floor, with prominent triangular facets and fault scarps present in alluvial fan deposits along much of the rangefront. The range-bounding fault forms a ~45 km long trace along the eastern flanks of the Pine Nut Range and Wellington Hills, and discontinuous scarps extend southward on this trend for ~30 km toward Sweetwater Flat (Figure 2). The part of the fault near the Wellington Hills forms a horsetail splay with numerous 5–10 m high east facing scarps. North from here to the Artesia Fan the fault trace is very linear and northwest striking, interrupted by two ~1 km wide right-steps. Along the northwest striking
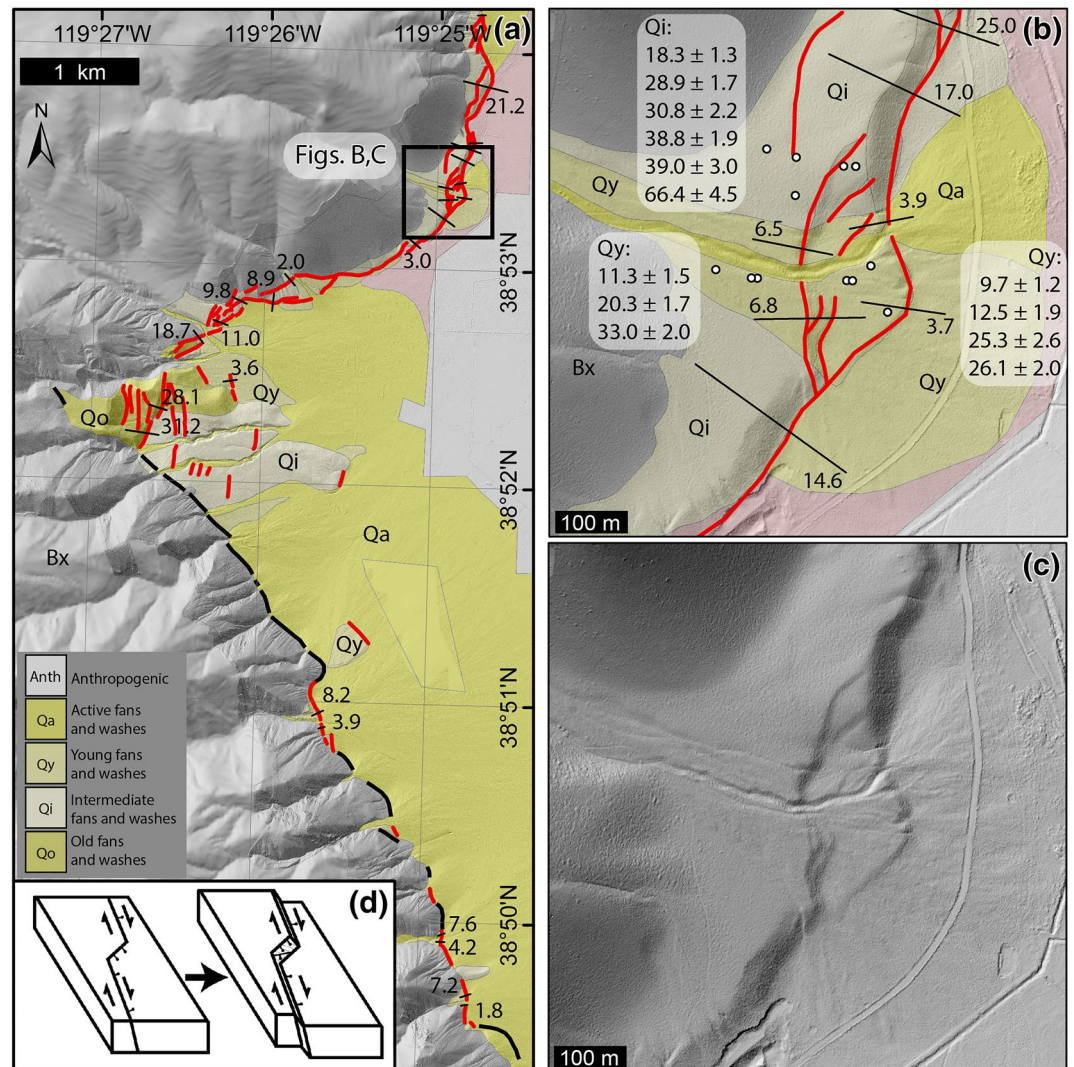
Figure 5. Section of Smith Valley rangefront showing (a) geometry of large right step and (b, c) location of Artesia fan slip rate site. Black faults are bedrock-alluvial fault contacts, while red faults are fault scarps in alluvial deposits. Values in (a) are scarp heights (in m). (b) Artesia fan rate site interpreted and (c) bare lidar hillshade. Scarp profiles, heights (in m), and ages (ka) of boulder samples (white dots) are shown in (b). (d) Simplified block diagram of a right-bend in a right-lateral oblique fault system provided to explain relatively larger vertical displacements in the step.

Table 2
Fault Slip Rates

	Offset (m)	Mean age[a] (ka)	Vertical rate (mm/yr)	Dip parallel (55 ± 10° normal fault) (mm/yr)	Extension (mm/yr)	Strike-slip (mm/yr)	GPS extension[b] (mm/yr)	GPS strike-slip[b] (mm/yr)
Artesia Qy	10.5 ± 0.1	19.7 ± 8.9	$0.5 \, ^{+0.7}/_{-0.2}$	$0.6 \, ^{+0.9}/_{-0.2}$	0.4 + 0.5/_0.1	?	0.4 ± 0.5	0.5 ± 0.4
Artesia Qi	19.5 ± 4.5	37. ± 16.3	$0.6 \, ^{+0.8}/_{-0.4}$	$0.7 \, ^{+1.0}/_{-0.5}$	0.4 + 0.6/-0.3	?	0.4 ± 0.5	0.5 ± 0.4
Antelope Valley	27.5 ± 4.3	62.4 ± 23.8	$0.5 \, ^{+0.5}/_{-0.3}$	$0.6 \, ^{+0.6}/_{-0.4}$	0.4 + 0.4/_0.2	–	0.7 ± 0.5	1.1 ± 0.4
Mason Valley	6.5 ± 3.6	$173.1 \, ^{+38.7}/_{-32.5}$	0.05 ± 0.01	0.06 ± 0.01	0.04 ± 0.01	–	0.6 ± 0.5	0.4 ± 0.4
Pine Grove Hills	18–33	40–60?	–	–	–	0.3–0.8	0.2 ± 0.6	0.6 ± 0.5
Wassuk/Walker Lake	13.5	14.5	$0.8 ± 0.2^{c}$	–	–	1.0^{d}	0.7 ± 0.3	0.6 ± 0.4

[a]Mean ages are not used for rate calculations but are provided here for reference. See text for details. [b]From Bormann et al. (2016). [c]From B. Surpless and Kroeger (2015). [d]From Dong et al. (2014).

sections, scarps are generally on the order of ~6–8 m in height (Figure 5), and less frequent, compared with the scarps in the northeast striking step-overs that are nearly continuous and have heights that frequently exceed 20 m. North of the Artesia Fan, the fault scarps are less frequent and more northerly striking, cutting mostly young and intermediate fan deposits. Nowhere along the fault trace did we observe laterally displaced stream channels, terrace risers, or fan apices. Wesnousky and Caffee (2011) excavated a paleoseismic trench across the rangefront fault near Wellington (Figure 2). The trench revealed evidence of a single earthquake at ~3,530 cal yr BP, with a vertical displacement of 3.5 m.

4.2.2. Fault Slip Rate

At the Artesia Fan is a series of three progressively faulted alluvial fan surfaces (Figure 5a). In Figure 5b: Qa are the active alluvial fan deposits, forming a narrow active channel cut into young Qy deposits, and on the basin floor form a small fan overtopping Qy deposits. These Qy deposits form an alluvial fan on the hanging wall of the fault as well as on the margins of the main Qa channel on the footwall, and are composed of light gray, rounded, unweathered granitic boulders in a poorly sorted matrix. Intermediate Qi deposits are only found on the footwall of the fault and are redder in color, with a smoother, less bouldery surface than Qy. The fault has an anastomosing pattern in Figure 5b that, from south to north, starts as a single strand, splits into two, then three strands, before coalescing into a single strand again. A maximum bound on the age of the Qi fan is provided by an underlying 60–80 ka tephra exposed in a road cut in the fault scarp (Stauffer, 2003; Wesnousky & Caffee, 2011). We collected 10 boulder samples for ^{10}Be analysis on the Qi and Qy displaced alluvial fan units and combined these with three recalculated ^{10}Be boulder ages at this site from Wesnousky and Caffee (2011) (Figure 5b). Six boulder samples were collected from the footwall of the intermediate unit (Qi, Figure 5b), and range in age from 18 to 66 ka (mean age of 37.0 ± 16.3 ka), and seven samples from both the hanging and footwalls of a younger aged alluvial fan unit (Qy, Figure 5b) range in age from 10 to 33 ka (mean age of 19.7 ± 8.9 ka) (Table 1). While these ages are scattered, the mean ages of the young surface are roughly half of that from the intermediate surface (Table 2). The average of four profiles measured from the lidar data (Figure 5) show that the scarp height of the single strand that cuts the intermediate unit is 19.5 ± 4.5 m, while two profiles of each of the two scarps in the younger unit measure 3.8 ± 0.1 and 6.6 ± 0.2 m, respectively, or 10.5 ± 0.1 m combined (Figure 5). Dividing these scarp heights by the ages of the boulder samples from each surface leads to a vertical separation rate of $0.6 \, ^{+0.8}/_{-0.2}$ mm/yr for the intermediate surface and $0.5 \, ^{+0.7}/_{-0.2}$ mm/yr for the young surface (Figure 4). These two rates over different timescales generally agree, and correspond to dip parallel rates of $0.7 \, ^{+1.0}/_{-0.5}$ and $0.6 \, ^{+0.9}/_{-0.2}$ mm/yr for the Qi and Qy surfaces, respectively (Table 2). All of these rates are higher than the 0.125–0.33 mm/yr rate reported by Wesnousky and Caffee (2011) for the same Qi surface, as their maximum rate is based on the assumption that the maximum measured cosmogenic age (CWL-4: ~60 ka) is a minimum age for the faulted surface, ignoring possible inheritance. The additional ages presented here suggest that this surface is younger than this single older outlier, and thus our slip rate is greater.
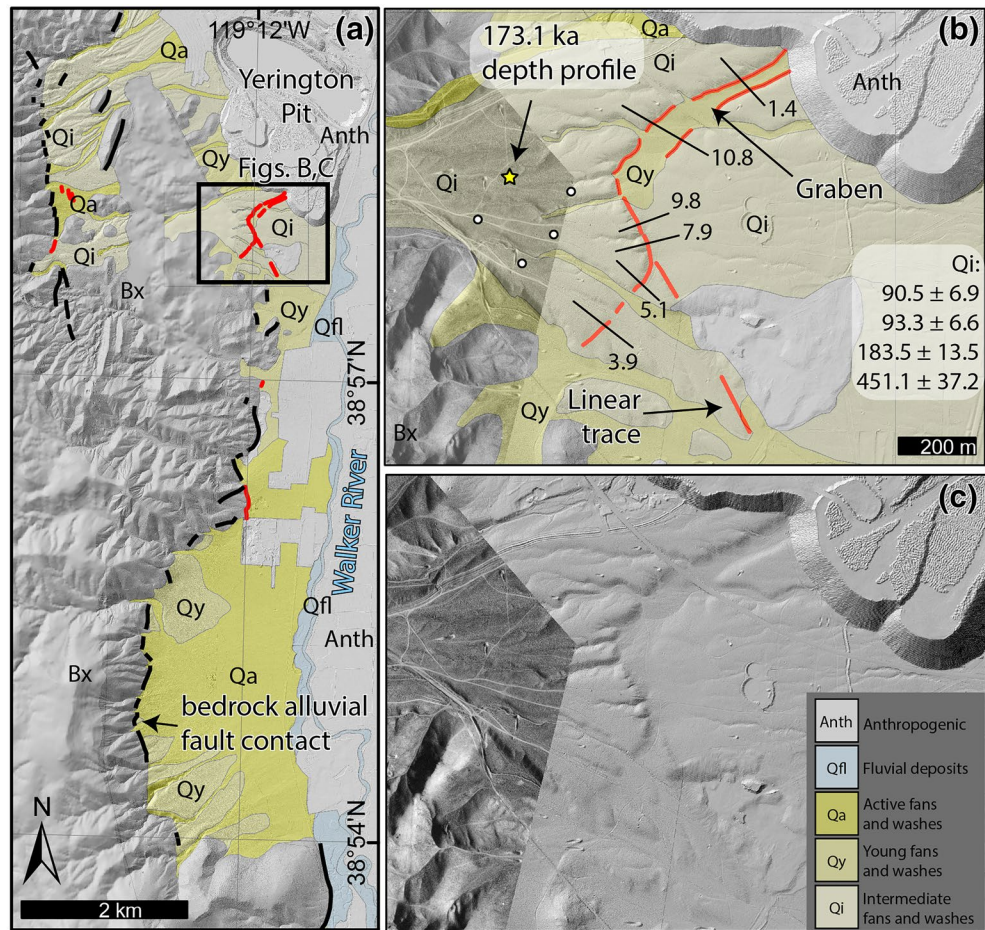
Figure 6. Section of Mason Valley rangefront showing (a) lack of fault scarps preserved in alluvium (red) and (b) location of Yerington fan slip rate site. (b) Yerington fan rate site interpreted and (c) bare lidar hillshade/low sun angle aerial photo composite. Scarp profiles, heights (in m), and ages (ka) of boulder samples (white dots) are shown in (b), while the age and location of the depth profile (Figure 7) is indicated by the star.
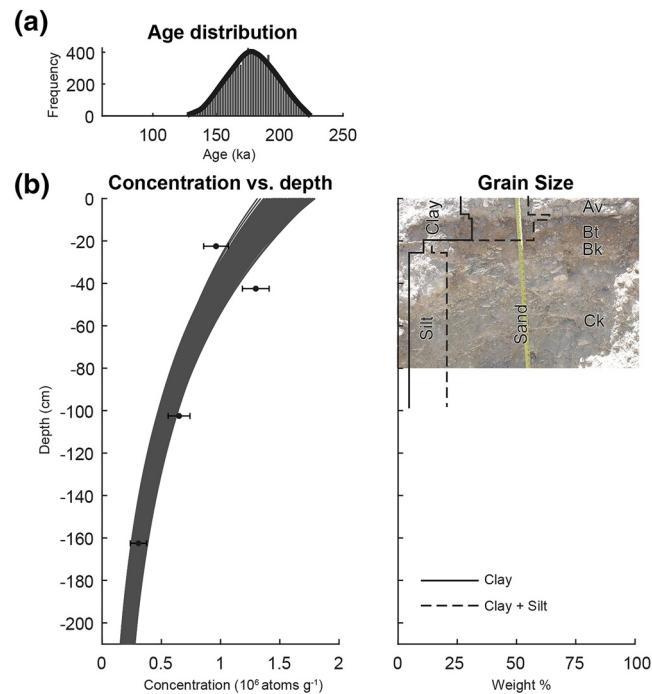
4.3. Mason Valley

4.3.1. Geomorphic Expression of Active Faulting

In contrast with the two previously described basins, the rangefront along the Singatse Range is more subdued, with only ~700 m of total relief above Mason Valley. Though there are triangular facets along the rangefront, there are few places where fault scarps are preserved in Quaternary deposits (Figure 6). The range-bounding fault extends from ~5 km south of where the West Fork of the Walker River enters the basin northward for ~35 km, forming a sinuous trace of both left- and right-steps between mostly north striking rangefront sections.

4.3.2. Fault Slip Rate

Adjacent to the Yerington Pit (Figure 6) a northwest striking fault scarp merges with a northeast striking fault scarp to form a large northeast striking graben cutting intermediate age alluvial fan deposits (Figure 6). This alluvial fan is incised up to ~6 m by channels and forms broad smooth interfluve surfaces with infrequent highly weathered granitic and volcanic boulders. Depending on where fault profiles are measured (Figure 6), vertical separation varies from as little as 1.4 m across the graben at the northeastern extent of the fault scarp to as much as 10.8 m, with an average of 6.5 ± 3.6 m for the six profiles. Based on the ~35 km length of the fault, this scarp could be the result of only 2–3 earthquakes (Wesnousky, 2008),

Figure 7. Results for the Mason Valley depth profile sampled at the Yerington fan, modeled using the Hidy et al. (2010) MATLAB code. The resulting age is 173.1$^{+38.7}$/$_{-32.5}$ ka. (a) Distribution of modeled results for the age of the depth profile. (b) Monte Carlo solutions (left) of concentration of ^{10}Be versus depth and soil textural analysis with well-developed Bt horizon (right) overlain on a photograph of the upper portion of the depth profile.

which may not be sufficient to account for variations in the seismic cycle (e.g., Styron, 2019). Here, we collected a depth profile of four samples as well as four surficial boulder samples for cosmogenic ^{10}Be analysis to constrain the age of the faulted surface. Boulder ages sampled from the Qo surface here range from 90.5 ± 6.9 ka to 451.1 ± 37.2 ka (mean of 204.6 ± 169.9 ka), and modeling the depth profile results in an age of 173.1 $^{+38.7}$/$_{-32.5}$ ka (Figure 7). The upper two samples in the depth profile do not fit the modeled curve, which could be a result of bioturbation. Were the uppermost sample discarded, the modeled age of the surface would be older. The well-developed soil, with a 10-cm thick Bt horizon, (Figure 7b), suggests a mid to late Pleistocene age, consistent with the modeled age of the depth profile (e.g., Angster et al., 2019; Birkeland, 1984). Dividing the 173.1 $^{+38.7}$/$_{-32.5}$ ka age of the depth profile by the 6.5 ± 3.6 m average displacement of the surface results in a vertical slip rate of <0.05 mm/yr. This rate correlates with extension and downdip slip rates of <0.04 and < 0.06 mm/yr, respectively. As this site is situated on the eastern side of a 2-km-wide left stepover (Figure 6a), some slip may be missing from this rate. However, we do not see evidence of youthful faulting along the western fault strand.

4.4. Pine Grove Hills

4.4.1. Geomorphic Expression of Active Faulting

The character of rangefront faulting south of Mason Valley abruptly changes ~5 km south of where the west fork of the Walker River enters the southwestern margin of the basin (Figure 2). This area is here referred to as the Pine Grove Hills, and instead of forming a rangefront composed of sharp triangular facets, the rangefront is subdued and is composed of a series of uplifted old alluvial fans and pediments. This fault zone is partly mapped as a normal fault in the USGS Quaternary fault and fold database, but new observations presented below increase the detail of mapping and show that it has a significant dextral strike-slip component. Here, Google Earth imagery and lidar data show a discontinuous series of linear, northwest-striking faults and lineaments that extend southeast for ~22 km. Generally, these faults have a northeast down sense of motion, and locally dextrally displace fan deposits and channels.
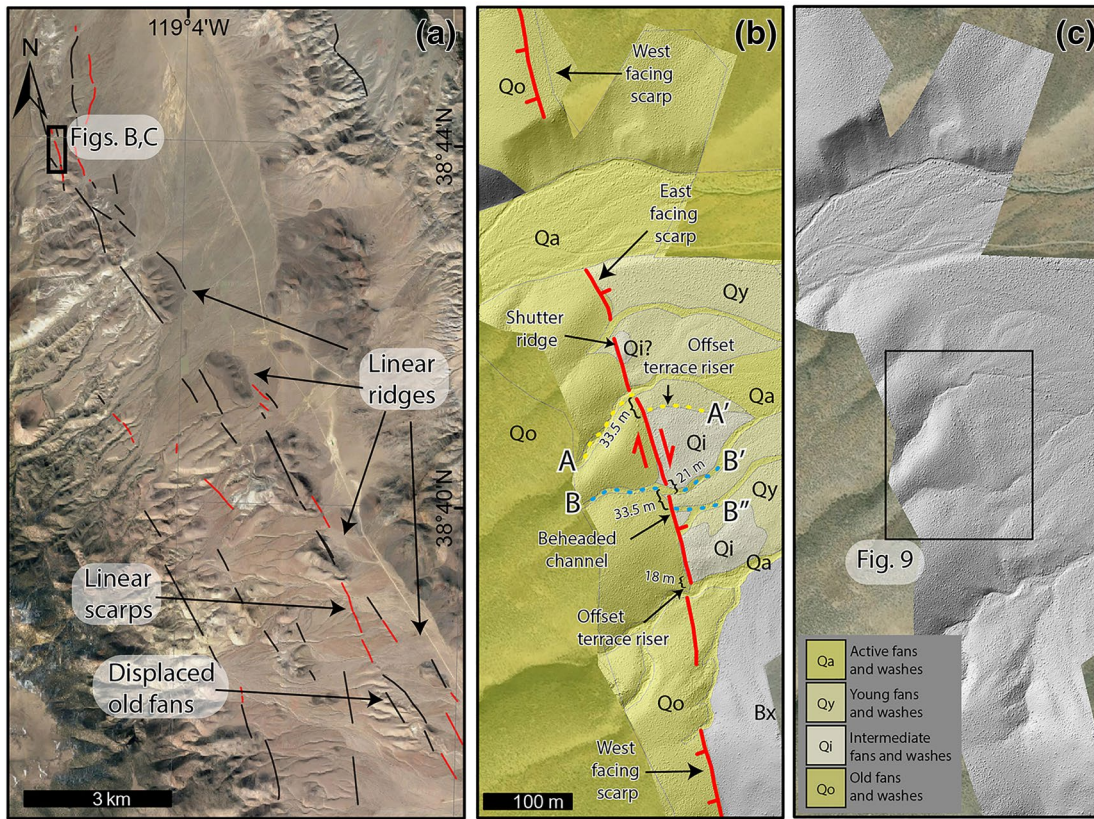
Figure 8. (a) Google Earth image of the Pine Grove Hills fault zone in southern Mason Valley. Location indicated in Figure 2. Red lines indicate faults in alluvial deposits, while black are fault traces in bedrock. (b) An interpreted SfM model, with stream offsets (dotted colored lines) and stream labels used in Figure 9 for reconstructions. (c) A section of this fault zone that demonstrates right-lateral displacements.

Several subparallel fault traces are well expressed as a series of linear bedrock ridges and scarps in different ages of alluvial fans (Figure 8a, Plate 1). These faults form distinct tonal and topographic lineaments that in many cases can be traced from scarps in alluvial fan surfaces along both margins of elongate, northwest oriented bedrock ridges that outcrop near the center of the valley. The linear bedrock ridges are primarily composed of Mio-Pliocene sedimentary and volcanic rocks, including the Morgan Valley and Coal Valley formations (R. E. Anderson et al., 2012; Gilbert & Reynolds, 1973).
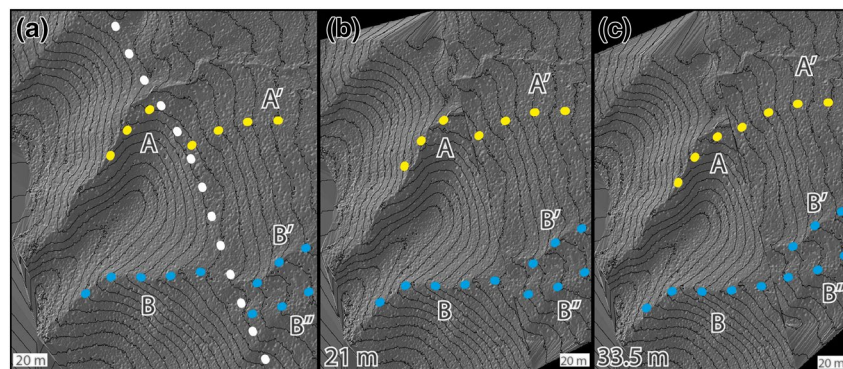
Figure 9. (a) Reconstructions of offsets from Figure 8 shown with 1.5 m contours and hillshaded SfM model. Dotted colored lines indicate features A and B. (b) 21 m of offset align stream B-B'. (c) 33.5 m of offset to align terrace riser A-A' and stream channel B-B".

4.4.2. Fault Slip Rate

Figure 8b is a Quaternary map based on a hillshade of a 0.25 m/pixel resolution structure-from-motion model (Figure 8c) where a linear fault trace dextrally displaces Qy and Qi deposits. From north to south along this section of the fault is a small shutter ridge, a ~33 m dextrally displaced Qi terrace riser (A′ in Figures 8b and 9c), a ~21 m dextrally deflected Qy channel (B′ in Figures 8b and 9b), a ~33 m dextrally displaced beheaded channel (B″ in Figures 8b and 9c), and a ~20 m dextrally offset terrace riser. To show these displacements, channels A and B are backslipped 21 and 33.5 m in Figures 9b and 9c, respectively. The direction of the scarp produced by the fault changes from a subdued west-facing scarp, to a clear east facing scarp, and back to a subdued west-facing scarp along strike, further demonstrating the strike-slip nature of this fault (McCalpin, 2009; Sylvester, 1988). A maximum age of the Qi terrace risers can be estimated by the correlative ~40–60 ka Qi surfaces measured in Antelope and Smith Valleys (Figures 3–5). Dividing the measured 18–33 m displacements by this age range results in a minimum slip rate for the Pine Grove Hills fault of 0.3–0.8 mm/yr. The geomorphology of this fault zone, including its length, discontinuous expression, scarcity of well-preserved lateral offsets, and subdued linear morphology, is similar to other dextral faults in the region with rates of this magnitude (e.g., Angster et al., 2019).
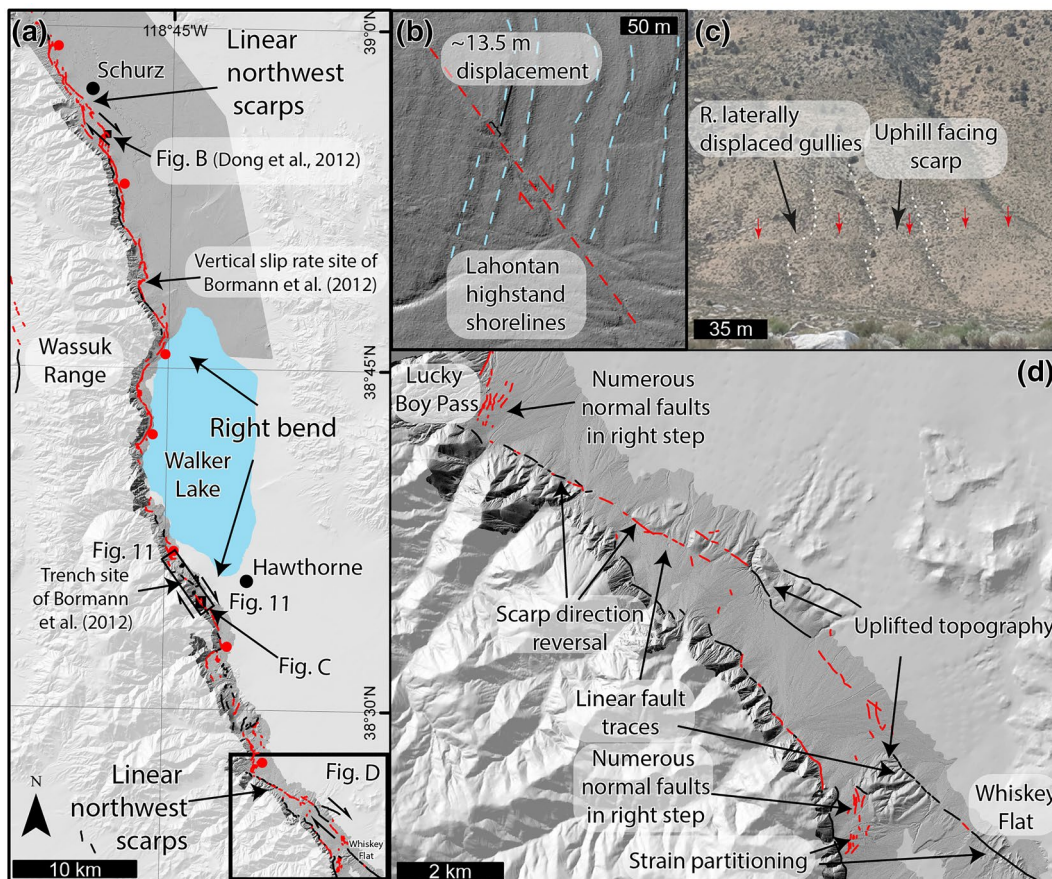
Figure 10. Fault map (a) of the Wassuk fault zone. Lidar hillshades are darker gray, light gray background is a hillshaded 10 m DEM. Red lines are fault scarps in alluvial deposits, black are inferred and/or bedrock-alluvial fault contacts. The fault geometry forms two northwest striking segments separated by a large right step coincident with Walker Lake and the deepest part of the basin. The northwest striking segments contain alternating scarp directions, linear scarps, and right-lateral displacements, all consistent with strike-slip faulting. Right-stepping segments locally exhibit greater degrees of normal faulting. Locations of (b–d) are indicated on (a). (b) Blowup of site from Dong et al. (2014) showing 13.5 m right-lateral displacement of ~14.5 ka Lahontan shorelines with slip rate of ~1 mm/yr. (c) Field photo of fault near Hawthorne where an uphill facing linear scarp right-laterally deflects a series of channels, note that scale applies to the rangefront, not the fan in the foreground. This section is also shown in Figure 11c. (d) The southern portion of the Wassuk fault zone. Here strain is partitioned into a linear basin-ward strike-slip fault and a normal fault against the range.
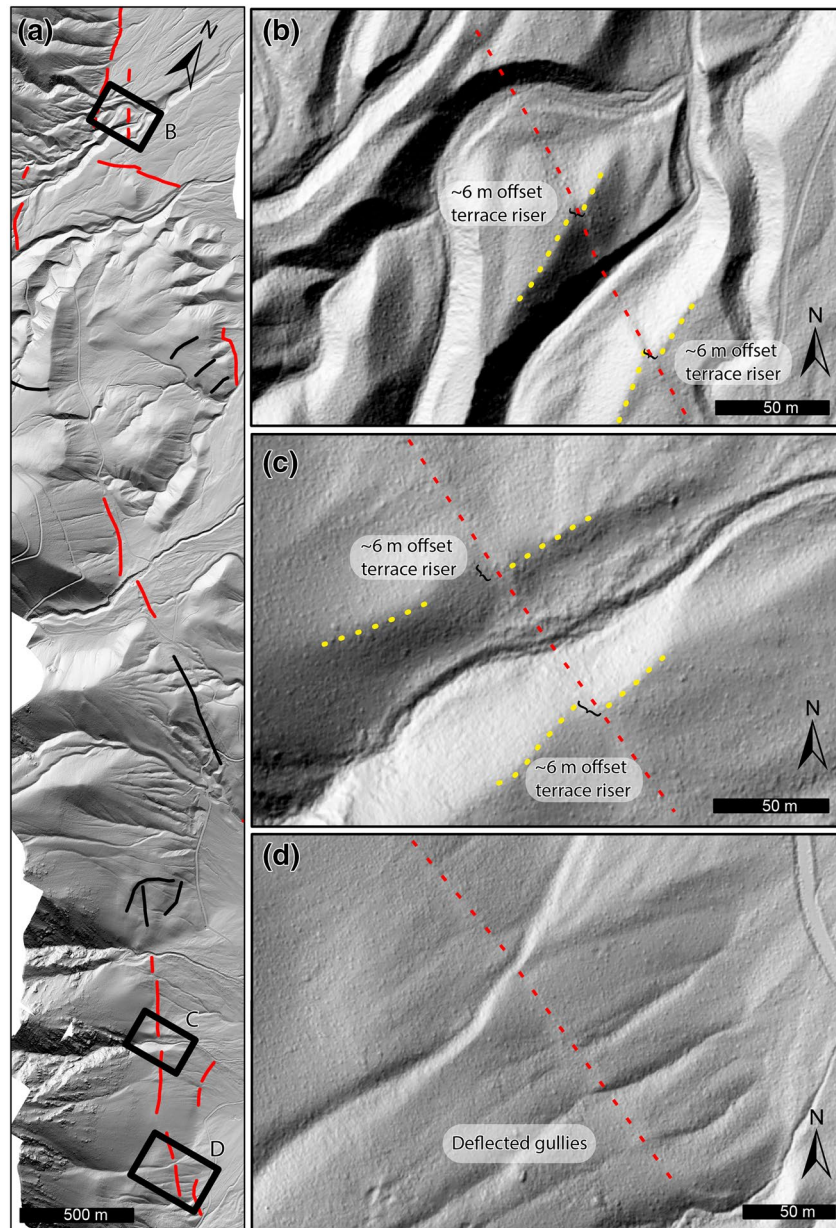
Figure 11. (a) Lidar hillshade of portion of the Wassuk Rangefront (b, c) west of Hawthorne showing strike-slip offsets of terrace risers and (d) gullies. Faults are red and dotted lines trace offset features. Note that (a) is rotated from north. Location of (a) indicated in Figure 10a. Photograph in Figure 10c is of the gullies in (d).

4.5. Walker Lake Basin

The Walker Lake basin (Figure 10) is the largest basin of those examined and is ∼100-km-long by 20-km-wide. The western margin of the basin is bound by the Wassuk range, which hosts a prominent, active, east-dipping, normal fault, forming more than 2,200 m of vertical relief. The vertical slip rate (>0.3–0.4 mm/yr) and paleoseismic history of this fault zone are described by Bormann et al. (2012) and B. Surpless and Kroeger (2015). Dong et al. (2014) document an active strike-slip fault in the northern part of the basin that displaces Lahontan aged shoreline deposits at a dextral slip rate of ∼1 mm/yr (Figure 10b). This strike-slip fault segment is partitioned away from the rangefront normal fault (Figure 10a). Here, observations are focused on additional evidence of strike-slip faulting and fault geometry along the central and southern portion of the fault (Figure 10).

Based on variations in strike, the Wassuk rangefront fault is here divided into three sections. From north to south: a linear northwest striking section extending northwest from near Schurz, a central sinuous roughly north and northeast striking section along the western shore of Walker Lake, and a southern northwest striking linear section from Hawthorne to Whiskey Flat (Figure 10a). The central section forms a right-step in the fault system. The deepest portion of the basin, Walker Lake, is located in this right-step. This geometry of the Walker Lake fault system has been previously described as a rhomboidal pull-apart in a strike-slip system (Mann, 2007), with Walker Lake itself situated in the depocenter of this pull-apart (Link et al., 1985).

Directly west of Hawthorne (Figure 11) is a generally NW-trending, discontinuous fault section with occasional uphill-facing scarps. This fault right laterally displaces both left and right terrace risers ~6 m at two different drainages (Figures 11b and 11c) and a series of gullies (Figures 10c and 11d). From this area south to Lucky Boy Pass (Figure 10d), the fault forms a right-stepping pattern of north and northeast trending normal fault scarps and northwest trending linear scarps.

From Lucky Boy pass to the southeast is a linear northwest striking fault section that extends for ~10 km (Figure 10d). The northern ~3 km of this fault section forms NNE facing fault scarps along the rangefront. Southward from here, the fault bifurcates into a rangefront fault and a linear, basin-ward strike-slip fault trace that forms subdued uphill-facing fault scarps. The basin-ward fault section features south and north facing scarps and prominent pop-up, pressure ridge-like features of uplifted bedrock, fan, and pediment surfaces (Figure 10d). The rangefront fault to the south of the basin-ward strike-slip fault gradually bends to be more northerly striking and forms a number of east-facing scarps at canyon mouth drainages. The faulting mapped in Figure 10d is an example of strain partitioning: where a basin-ward strike-slip fault is separated from a rangefront normal fault (similar to Figure 10b and Dong et al., 2014).

The ~30-km-long series of fault scarps extending from the southern margin of Walker Lake to Whiskey Flat (Figure 10d) are generally northwest trending. Normal scarps in north-trending bends are more numerous than those observed along the northwest-trending linear sections. The linearity of the fault traces, the alternating-facing fault scarps (Figures 10c and 11), and the several beheaded channels and lateral displacements in the northwest-striking portions of the fault zone (Figure 11), and the magnitude of scarps in the north-striking right-steps are all interpreted to be a result of northwest directed dextral faulting.

5. Geodetic Analysis and Kinematic Efficiency

To understand how shear accommodation in the Central Walker Lane differs from shear accommodation in the Northern and Southern Walker Lane, we need first need to constrain shear budgets spanning the length of the Walker Lane. Although many recent studies have presented geodetic budgets for individual sections of the Walker Lane (e.g., Bormann et al., 2016; Hammond et al., 2011; Z. M. Lifton et al., 2013; Pardo et al., 2012), these studies present GPS velocities determined using data from different time spans and processed using different algorithms, postseismic corrections, and reference frames, which makes it difficult to determine whether differences in geodetic shear budgets are the due to changes in the deformation field or differences in data processing methods. The most recent analysis of GPS velocities spanning the entire Walker Lane system from north to south is presented in Bennett et al. (2003), dating from a time when the field of GPS geodesy was in its relative infancy and GPS stations were sparse.

In Figure 12, we present a series of 5 GPS velocity profiles illustrating the increase in interseismic GPS velocity magnitude relative to the North America along 350-km-long and 50-km-wide transects spanning the Basin and Range, Walker Lane, and Sierra Nevada transition (see Figure 13a for profile locations and extent). The velocity profiles are oriented N39°E, perpendicular to the GPS observed orientation of maximum horizontal shear strain for the Walker Lane, to capture the maximum shear deformation budget. The profiles show a steeper velocity gradient across the Walker Lane than in the neighboring Sierra Nevada microplate to the west or slowly extending Basin and Range province to the east. In all profiles, the velocities increase smoothly in a single steep ramp across the Walker Lane, and the profiles do not show discrete

steps in associated with individual faults. A smooth velocity field is an expected feature of a GPS velocity field measuring interseismic deformation above locked faults where the fault spacing is less than twice the locking depth. Shear deformation budgets for each profile are determined by subtracting the velocity of GPS stations just east of the Walker Lane in the Basin and Range, from the velocity of GPS station on the Sierra Nevada microplate to the west (horizontal blue dashed lines in Figure 12). The total shear budget across the Walker Lane decreases from ~10 mm/yr in the south (Profile E) to ~6 mm/yr in the north (Profile A).

The geodetic shear budgets determined from the velocity profiles shown in Figure 12 provide the basis to quantify the discrepancy between geologic and geodetic measurements of shear in the Walker Lane. We evaluate the discrepancy using the concept of kinematic efficiency, which, as defined by Hatem et al. (2017), is the ratio of total on-fault deformation to total shear. We sum the published geologic dextral fault slip rates with those determined in this study for each profile (Table 3) and divide this sum by the geodetic shear budget for that profile to calculate kinematic efficiency percentages shown in Figure 13a. These relations are also illustrated graphically by the red stepped cumulative slip rate functions in Figure 12. For simplicity, and due to both the uncertainty of fault geometry and limited contribution to northwest-oriented-shear, normal faults and transverse faults are omitted from this analysis. In general, the geologic rates reported in Table 3 are the highest rates resulting from the most recent publications. By examining shear in this way, we can make direct comparisons to the results of laboratory experiments.

Here we briefly summarize the observations of this kinematic efficiency analysis, from south to north (Figure 12). In Profile E, the Airport/Little Lake Valley, Panamint Valley, Death Valley, and Stateline faults together sum to ~9.1 mm/yr, ~90% of the 10 mm/yr of dextral shear observed by geodesy (Figure 12e). Profile D only crosses the White Mountains and Fish Lake Valley faults with a combined rate of 6.5 mm/yr, ~80% of the 8 mm/yr observed geodetically (Figure 12d). This may be a high estimate as there are several rates for the Fish Lake Valley fault in Frankel et al. (2011) that are lower than the 6.1 mm/yr rate used here. In Profile C, the Wassuk rangefront fault, along with the Gumdrop Hills, Indian Head, Benton Springs, and Petrified Springs strike-slip faults, have a summed rate of 4.8, ~60% of the 8 mm/yr observed geodetically (Figure 12c). In Profile B, across the western part of the Central Walker Lane, the Pine Grove Hills fault and the Wassuk rangefront faults are the only known dextral strike-slip faults, with a total rate of 1.6 mm/yr, only 25% of the 7 mm/yr observed in the geodetic profile (Figure 12b). Profile A crosses the Polaris, Warm Springs, Honey Lake, Pyramid Lake, and Mohawk Valley strike-slip faults with a combined rate of 3.8 mm/yr, ~60% of the 6 mm/yr observed by geodesy (Figure 12a). All together, these kinematic efficiencies vary from ~25% to 90%.

6. Discussion

6.1. Summary of Evidence of Lateral Motion in the Central Walker Lane

Only along the Wassuk rangefront and Pine Grove Hills faults were we able to find dextrally displaced piercing points. In Smith Valley, the rangefront geometry of linear, optimally oriented northwest striking fault sections separated by right-steps with increased scarp heights is similar to that of the Wassuk rangefront fault, and both fit a model of fault slip across a right-step with a significant oblique dextral component (e.g., Figure 5d). The Smith Valley fault trace is also much more linear than the other normal faults in this study, suggestive of lateral motion. While we were unable to locate any offset piercing points along this fault, any offset markers may have been buried by alluvial fan activity in the 3,530 years following the most recent earthquake (Wesnousky & Caffee, 2011).

These faults provide different examples of how dextral shear is accommodated in this region. In both Smith Valley and the Walker Lake Basin, shear is accommodated in part by large right-steps along oblique slipping rangefronts. The Pine Grove Hills fault is a primarily dextral strike-slip fault with little relative vertical motion, as demonstrated by the opposite facing scarp directions, subdued topography, and comparably large dextral offsets (Figure 8b). The oblique slipping Wassuk rangefront displays evidence of both strain partitioning and bi-modal fault behavior, where a single fault can produce either lateral or vertical slip in different earthquakes (e.g., Barnhart et al., 2015). In some locations along the Wassuk range fault system, strain is partitioned between the rangefront normal fault and a separate dextral fault outboard of the rangefront (e.g., Figure 10b). In other places dextral offsets are expressed on the rangefront as uphill facing scarps and deflected streams (e.g., Figures 10c and 11d). Repetition of events that produced these strike-slip features
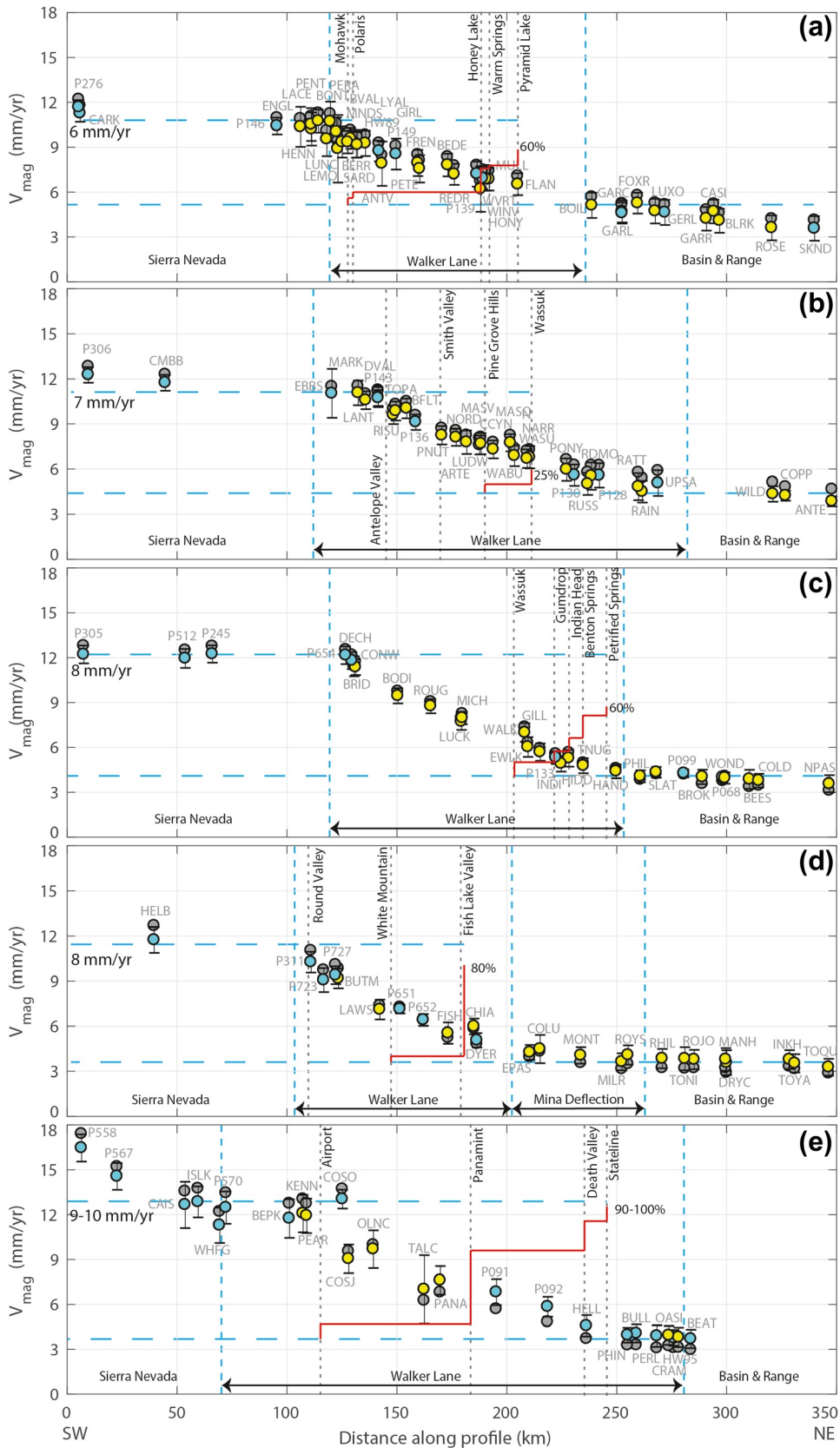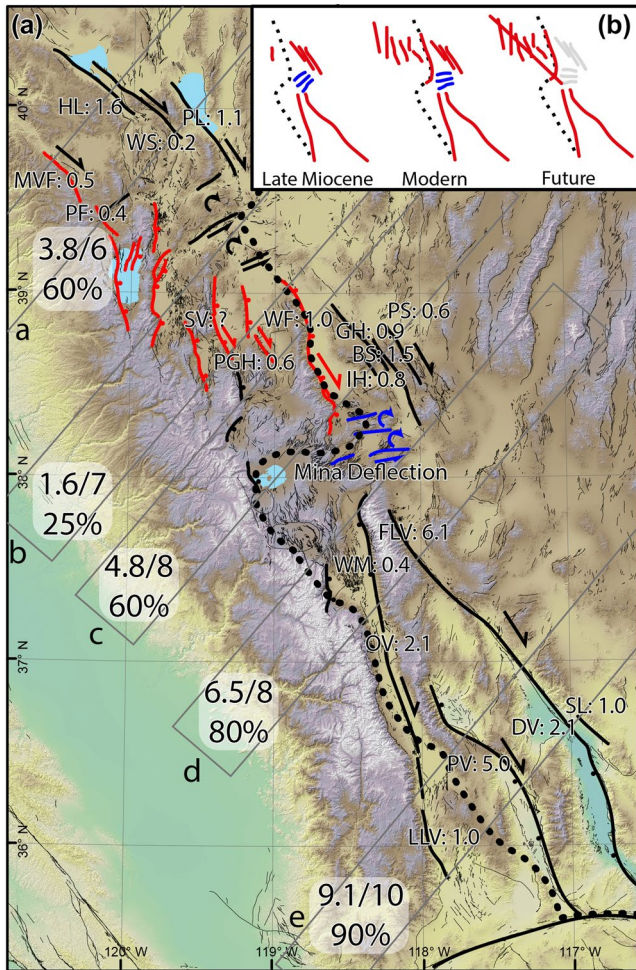
Figure 13. (a) Major faults of the Walker Lane are bold, with faults of the western Central Walker Lane in red and the Mina Deflection in blue. Dotted black line is the approximate extent of the Sierra Nevada batholith (modified after Long, 2019). Arrows indicate motions or rotations of faults and blocks. Ratios (*x/y*) are a comparison of the sum of the individual geologic rates (*x*) measured across the Walker Lane in various profiles (gray boxes, a–e) to the GPS rates (*y*) for each profile. Percentages are the geologic rate divided by the GPS rate. Smaller numbers are dextral strike-slip rates of individual faults in mm/yr (fault names and slip rate sources listed in Table 3). There is good agreement between geodetic and geologic observations in the Southern Walker Lane, but less so in the Central and Northern Walker Lane. (b) Model of structural evolution of the Sierra Nevada Basin and Range transition zone and the Central Walker Lane. Initially the edge of the Sierra Nevada batholith resisted deformation and dextral shear followed a right step at the Mina Deflection. Continued deformation rotated and strengthened the faults of the Mina Deflection. In the future, a through-going strike-slip fault may form as the Mina Deflection is no longer able to accommodate the right-step.

could not have simultaneously produced the steep rangefront, implying bi-modal earthquake behavior.

6.2. Comparison of Geologic Rates to Block Models

The vertical separation rates and resulting extension and dip-parallel slip rates for the Walker Lake, Pine Grove Hills, and Mason, Smith, and Antelope valley faults are listed in Table 2 along with the block modeled rates for the same faults from Bormann et al. (2016). The extension rates for all faults except Mason Valley are within the margins of error for both the geologic and geodetic methods. In Mason Valley, the geologic rate of <0.05 mm/yr is an order of magnitude less than the geodetic estimate of ~0.5 mm/yr. As the Singatse Range is much more subdued in topographic expression than other ranges in this region, and the rangefront generally lacks the uplifted, faulted fan surfaces common to the other faults in the region with slip rates of ~0.5 mm/yr, it seems that the much lower geologic rate is more accurate. This discrepancy could be a result of the block model regularization parameters that favor smooth and simple slip rate solutions (Bormann et al., 2016) not allowing sufficient variability to match the geologic partitioning of slip across the faults in the region.

The geologic dextral rate of ~1 mm/yr (Dong et al., 2014) for the Wassuk range is within the error of the 0.6 ± 0.4 mm/yr block modeled rate. The block model dextral rate of the Pine Grove Hills fault is 0.6 ± 0.5 mm/yr, encompassing the ~0.3–0.8 mm/yr estimate here. The geodetic right lateral strike-slip rate of 1.1 ± 0.4 mm/yr in Antelope Valley is among the fastest rates in the region, yet the fault lacks any observable geomorphic expression of dextral slip. The small faults sections on the east side of Antelope Valley with dextral displacements do not follow any major zone or structure as might be expected with a rate of this magnitude. In Smith Valley, the GPS block model predicts 0.5 ± 0.4 mm/yr of dextral strike-slip (Bormann et al., 2016). As the geologic rate was measured on the edge of a large right-bend that is nearly perpendicular to the overall trend of the rangefront fault (Figure 5), part of the ~0.4 mm/yr extension rate may be a result of a lateral component of motion along the fault, as predicted by the block model.

The sum of the block modeled dextral slip rates (Bormann et al., 2016) for the faults in Antelope, Smith, and Mason valleys, and the Wassuk rangefront, is 2.6 ± 1.6 mm/yr, spread across the faults in each of these basins (for the purposes of this transect Mason Valley and Pine Grove Hills are considered one fault). Geologically, we measure a total of ~1.5 mm/yr of dextral slip between the Wassuk rangefront and our estimate for the Pine Grove Hills, which could be as much as ~2.0 mm/yr if the extension measured in Smith Valley is attributed to dextral shear along the rangefront. In sum, there still remains some discrepancy between the predicted dextral rates from the block models and the geologic rates, however this discrepancy is less than previously thought (e.g., Wesnousky et al., 2012).

Figure 12. Profiles of GPS velocity magnitudes across the Walker Lane, see Figure 13 for locations. Gray dots are uncorrected for postseismic response, yellow dots are MAGNET stations, cyan are Plate Boundary Observatory stations (see supporting information for treatment of GPS data). Dashed horizontal blue lines show the velocity change across the Walker Lane, while vertical dashed blue lines show the approximate edges of the Sierra Nevada/Walker Lane/Basin & Range. Vertical dotted gray lines are the locations of major faults. Red stair stepping lines are representative of the cumulative strike-slip slip rates of faults from west to east. Percentages are the same as Figure 13: the cumulative slip rate in each profile divided by the GPS rate of each profile.

Table 3
Walker Lane Strike-Slip Rates

	Fault abrv.	Fault name	Geologic strike-slip rate (mm/yr)	Reference
Profile a	PF	Polaris	0.4	Hunter et al. (2011)
	WS	Warm Springs	0.2	Gold et al. (2013)
	HL	Honey Lake	1.6	R. D. Gold et al. (2017)
	PL	Pyramid Lake	1.1	Angster et al. (2016)
	MVF	Mohawk Valley	0.5	R. D. Gold et al. (2014)
Profile b	WF	Wassuk Rangefront	1.0	Dong et al. (2014)
	PGH	Pine Grove Hills	0.6	This study
	SV	Smith Valley	?[a]	This study
Profile c	BS	Benton Springs	1.5	Angster et al. (2019)
	GH	Gumdrop Hills	0.9	Angster et al. (2019)
	PS	Petrified Springs	0.6	Angster et al. (2019)
	IH	Indian Head	0.8	Angster et al. (2019)
	WF	Wassuk Rangefront	1.0	Dong et al. (2014)
Profile d	FLV	Fish Lake Valley	6.1	Frankel et al. (2011)
	WM	White Mountain	0.4	Kirby et al. (2006)
	OV	Owens Valley	2.1[a]	Haddon et al. (2016)
Profile e	PV	Panamint Valley	5.0	Choi (2016)
	DV	Death Valley	2.1	Frankel et al. (2015)
	SL	State Line	1.0	Guest et al. (2007)
	LLV	Little Lake Valley	1.0	Amos et al. (2013)

[a]Not included in calculations.

6.3. How Shear is Accommodated Without Major Strike-Slip Faults

Laboratory shear models of fault evolution and many field studies show that a large portion (often >20%) of total deformation is accommodated as off-fault deformation (e.g., Hatem et al., 2017; Herbert et al., 2014; Oskin et al., 2012; Personius et al., 2017). However, off-fault deformation is usually considered on a singular fault basis, not at a fault system scale (e.g., R. D. Gold et al., 2015). By considering the kinematic efficiency in profiles across the Walker Lane, as described above, we can estimate off-fault deformation across the entire fault system. The laboratory models of Hatem et al. (2017) show that even structurally mature through-going faults are only ~80% efficient, with ~20% of total shear accommodated by off-fault deformation, while immature faults, with limited total slip, can be less than 40% efficient, with >60% of the total shear accommodated off of faults. In the Walker Lane kinematic efficiencies vary from as little as ~25% in the Central Walker Lane (profile b in Figures 12 and 13a) to ~60% in the Northern and ~80%–90% in the Southern Walker Lane (profiles A, D, and E in Figures 12 and 13a).

The "off-fault" shear in the Central Walker Lane is likely accommodated by a combination of broad co-seismic warping, displacements that are not preserved in the paleoseismic record, and rotations of crustal blocks. Geologically accounting for near surface coseismic off-fault deformation generally requires detailed pre and postearthquake observations of a fault system, and is therefore difficult to account for in the paleoseismic record (e.g., R. D. Gold et al., 2015; Herbert et al., 2014; Milliner et al., 2015; Oskin et al., 2012; Personius et al., 2017). For example, Oskin et al. (2012) showed that during the 2010 M7.2 El Mayor-Cucapah earthquake multiple faults were linked by "enigmatic zones of distributed deformation." These zones did not rupture the surface, yet they accommodated a significant amount of strain.

Numerous small and moderate earthquakes (<M6) occur in the Walker Lane (e.g., Hatch et al., 2019; Ruhl et al., 2016), and while many of these such as the 2016 M5.6, M5.4, and M5.5 Nine-Mile Ranch sequence do not

rupture the surface, they do contribute to the regional geodetically observed shear (e.g., Bell et al., 2012; Hatch et al., 2019). Historical strike-slip ruptures in the Walker Lane and Eastern California Shear Zone including the 1932 M7.2 Cedar Mountain, 1992 M7.3 Landers, 1999 M7.1 Hector Mine, 2019 M6.4 & M7.1 Ridgecrest, and 2020 M6.5 Monte Cristo Range earthquakes all ruptured complicated patterns across numerous discontinuous fault segments (Barnhart et al., 2019; Bell et al., 1999; Koehler et al., 2021; Rockwell, 2000; Rubin & Sieh, 1997). Subsequent studies have shown that many of the respective seismogenic faults have recurrence times on the order of ~3–15 ka, and that, if present, scarps from prior events are heavily degraded (Bell et al., 1999; Rockwell, 2000; Rubin & Sieh, 1997). Many of the faults that accommodated these ruptures are neither major through-going structures nor range-bounding faults (Bell et al., 1999; Jobe et al., 2020; Koehler et al., 2021). We suggest that future M7 strike-slip events in the Central Walker Lane may be similar to these events, and might occur across a series of previously recognized and unrecognized structures.

As the lowest measured dextral slip rates in Figure 13a are ~0.4 mm/yr, this rate may represent the threshold of preservation for multiple event offsets on strike-slip faults in the Walker Lane. Below this slip rate, geomorphic processes likely outpace the rate at which faults displace landforms, so offsets are destroyed faster than displacements can accumulate. Thus, evidence of low slip rate faults might not be preserved in the landscape.

Both GPS block models (Bormann et al., 2016) and paleomagnetic studies (Carlson, 2017; P. H. Cashman & Fontaine, 2000) agree that clockwise vertical-axis block rotations play a significant role in strain accommodation in the Carson domain and Mina Deflection. However, the role of block rotations remains unclear in the western domain of the Central Walker Lane. GPS block models predict low rate vertical-axis clockwise block rotations of 1°/Myr that act in concert with oblique faulting to accommodate observed shear strain (Bormann et al., 2016). However, limited paleomagnetic measurements in the Singatse Range, Wellington Hills, and Buckskin Range of the western domain record statistically insignificant amounts of rotation, which suggests that these blocks may be purely translating (Carlson, 2017).

Thus, while not all of the shear across the Central Walker Lane can be accounted for by summing the slip rates of known strike- and oblique-slip faults, and some "on-fault" shear may not be preserved, the sum of the lateral slip rates of the individual faults need not necessarily equal the total geodetic shear across a fault system, as distributed shear, block rotations, and complex fault relationships can accommodate a significant portion of "off-fault" shear, especially in immature systems such as the Walker Lane. This presents a problem for fault based seismic hazard models, as we do not know exactly which faults might accommodate this shear in future earthquakes. In this context, in regions with complex distributed fault patterns it may be better to use geodetic strain observations to forecast future earthquake probabilities (e.g., Lamb et al., 2018).

6.4. Structural Evolution of the Central Walker Lane

Field studies and laboratory models show that as strike-slip systems increase in total displacement, the width of the shear zone decreases, while faults become longer, less complex, more continuous, and more efficient at accommodating strain (An & Sammis, 1996; Atmaoui et al., 2006; Aydin & Nur, 1982; Faulds et al., 2005; Hatem et al., 2017; Schreurs, 2003; Stirling et al., 1996; Wesnousky, 1988; Wilcox et al., 1973; Zinke et al., 2015; Zuza et al., 2017). However, fault complexity is not solely a result of total shear accumulated across a fault zone, and faults largely take advantage of preexisting crustal weaknesses (e.g., Aitken et al., 2013; Calzolari et al., 2016; Dyksterhuis & Müller, 2008; Matenco et al., 2007; Molnar, 1988; Raimondo et al., 2014; Ziegler et al., 1998).

The Wassuk range, along with the rest of the ranges to the west, form the easternmost margin of the Sierra Nevada batholith, which is a significant structural boundary (black dotted line in Figure 13: Buer et al., 2009; Long, 2019). The westward stratigraphic tilt of the ranges in the Central Walker Lane decreases to the northwest from 60° in the Wassuk and Singatse ranges, to <20° in the Carson Range, and <5° in the Sierra Nevada (B. E. Surpless et al., 2002). Likewise, the southeasterly Singatse and Wassuk ranges have considerably higher amounts of total extension (>150%) than the ranges to the west (B. E. Surpless et al., 2002), which has been cited as evidence of the progressive northwestward encroachment of faulting into the Sierra Nevada block.

The faults in the western part of the Central Walker Lane form a left-stepping en-echelon pattern that falls roughly on trend with the Death Valley-Fish Lake Valley fault (Figures 1 and 13), the longest and highest slip rate fault in the Walker Lane (Frankel et al., 2007). Interrupting the northernmost part of the Fish Lake Valley fault is the Mina Deflection (e.g., Nagorsen-Rinke et al., 2013; Wesnousky, 2005), which accommodates a right step-over to the faults of the eastern part of the Central Walker Lane (Figures 1 and 13). Based on both paleomagnetic data (Petronis et al., 2009) and the nonoptimal, nearly east-west orientations of the sinistral faults in the Mina Deflection (Wesnousky, 2005), the crustal blocks here have accommodated clockwise vertical axis rotations of ~20°–30°. As faults rotate, their orientations become progressively less favorable to slip, and based on Mohr Coloumb faulting theory approach a state of lockup (e.g., Hill & Thatcher, 1992; Scholz, 2019; Sibson, 1985; Thatcher & Hill, 1991). This lockup angle is ~2Θ, where Θ is the angle between the maximum compressive stress, σ_1, and the initial fault plane. Whether we assume that the faults in the Mina Deflection initially formed at Θ = ~30° from the roughly north-oriented σ_1 (e.g., Bellier & Zoback, 1995), based on Mohr Coulomb theory and Byerlee's law, or if they formed at Θ = ~45°, as Reidel shears perpendicular to the primary northwest oriented dextral faults (Wesnousky, 2005), their current 080°–085° orientation is close to the lockup angle, 2Θ. At this stage of rotation, modeling and field studies show that a new set of faults may form (e.g., Olive & Behn, 2014; Richardson & Seedorff, 2017).

In Figure 13b, we present a model of structural evolution for the Central Walker Lane that synthesizes (1) the westward encroachment of faulting in the Central Walker Lane, (2) the rotation of the Mina Deflection, and (3) the lack of through-going strike-slip faults in the western part of the Central Walker Lane. Initially, a rigid Sierra Nevada batholith resisted deformation, and dextral faulting followed the edge of the block with a large right step at the Mina Deflection. As shear continues to today, the sinistral faults accommodating this step-over have rotated and approached the theoretical lock-up angle, while simultaneously the eastern margin of the Sierra Nevada block has been fractured by faulting. In the final pane, the faults in the Mina Deflection have further rotated, "shutting off" the right step, and shear follows a more simple, linear, through-going strike-slip fault. This model provides an example of how a major step-over in a strike-slip system can be transient in time. Here a step-over is accommodated by block rotations, but as those blocks rotate, they become less able to accommodate the step-over, and faults instead break a new path.

7. Conclusions

We present new vertical slip rates of 0.6 $^{+0.7}/_{-0.3}$, 0.7 $^{+1.0}/_{-0.4}$, and <0.05 mm/yr for the Antelope, Smith, and Mason valley range-bounding normal faults, respectively. We estimate the dextral slip rate of the Pine Grove Hills fault to be 0.3–0.8 mm/yr, and we report new sites along the Wassuk Rangefront that accommodate dextral slip. The southern Wassuk and Smith Valley rangefronts in the Central Walker Lane accommodate previously unrecognized oblique slip, whereas in the Pine Grove Hills and northern Wassuks, discrete strike-slip faults accommodate slip. We present a series of geodetic profiles spanning the Walker Lane, showing that total shear rates decrease from 9 to 10 mm/yr at the latitude of Death Valley to ~6 mm/yr at the latitude of Honey Lake. Our new data show that the kinematic efficiency (here defined as the ratio of summed geologic strike-slip rates to the regional geodetic shear budget) of the Central Walker Lane is only 25%, significantly lower than the ~60% and ~90% observed in the Northern and Southern Walker Lane, respectively. The remaining unaccounted shear is presumed to be accommodated by off fault deformation, such as a combination of block rotations and faulting that are not preserved in the paleoseismic record. We present a model for the structural evolution of a crustal scale right-step in a dextral system that explains the present configuration of faulting in the Central Walker Lane. The model provides an explanation of how step overs might form in response to preexisting structural conditions but be bypassed as shear accumulates. The Central Walker Lane is an example of a region where the geologic rates of known structures underestimate the deformation rates derived from geodesy, and this might be expected in other regions characterized by broad zones of distributed deformation.

Data Availability Statement

The SfM data for the Pine Grove Hills are available on opentopography.org at https://doi.org/10.5069/G9H1306R. The 2006, 2009, and 2010 Walker River lidar data used are available by request using the contact details at https://coast.noaa.gov/inventory/. The 2015 lidar data collected for this research are available on opentopography.org at https://doi.org/10.5069/G95T3HJ8. Laboratory data and sample information used for calculation of cosmogenic ages are listed in Tables S1 and S2, and at https://doi.org/10.1594/PANGAEA.926418. The GPS data used are listed in Table S4 and at https://doi.org/10.1594/PANGAEA.926828.

References

Adams, K. D., & Wesnousky, S. G. (1998). Shoreline processes and the age of the Lake Lahontan highstand in the Jessup embayment, Nevada. *Geological Society of America Bulletin*, *110*, 1318–1332.

Aitken, A. R. A., Raimondo, T., & Capitanio, F. A. (2013). The intraplate character of supercontinent tectonics. *Gondwana Research*, *24*, 807–814. https://doi.org/10.1016/j.gr.2013.03.005

Amos, C.B., Brownlee, S. J., Rood, D. H., Fisher, G. B., Burgmann, R., Renne, P. R., & Jayko, A. S. (2013). Chronology of tectonic, geomorphic, and volcanic interactions and the tempo of fault slip near Little Lake, California. *Geological Society of America Bulletin*, *125*, 1187–1202. https://doi.org/10.1130/B30803.1

An, L.-J., & Sammis, C. G. (1996). Development of strike-slip faults: Shear experiments in granular materials and clay using a new technique. *Journal of Structural Geology*, *18*, 1061–1077. https://doi.org/10.1016/0191-8141(96)00012-0

Anderson, R. E., Berger, B. R., & Miggins, D. (2012). Timing, magnitude, and style of Miocene deformation, west-central Walker Lane belt, Nevada. *Lithosphere*, *4*, 187–208. https://doi.org/10.1130/L174.1

Angster, S., Wesnousky, S., Figueiredo, P., Owen, L. A., & Hammer, S. (2019). Late Quaternary slip rates for faults of the central Walker Lane: Spatiotemporal strain release in a strike-slip fault system. *Geosphere*, *15*, 1460–1478.

Angster, S., Wesnousky, S., Huang, W., Kent, G., Nakata, T., & Goto, H. (2016). Application of UAV photography to refining the slip rate on the Pyramid Lake fault zone, Nevada. *Bulletin of the Seismological Society of America*, *106*, 785–798. https://doi.org/10.1785/0120150144

Atmaoui, N., Kukowski, N., Stöckhert, B., & König, D. (2006). Initiation and development of pull-apart basins with Riedel shear mechanism: Insights from scaled clay experiments. *International Journal of Earth Sciences*, *95*, 225–238. https://doi.org/10.1007/s00531-005-0030-1

Aydin, A., & Nur, A. (1982). Evolution of pull-apart basins and their scale independence. *Tectonics*, *1*, 91–105. https://doi.org/10.1029/TC001i001p00091

Balco, G., Stone, J. O., Lifton, N. A., & Dunai, T. J. (2008). A complete and easily accessible means of calculating surface exposure ages or erosion rates from ^{10}Be and ^{26}Al measurements. *Quaternary Geochronology*, *3*, 174–195. https://doi.org/10.1016/j.quageo.2007.12.001

Barnhart, W. D., Briggs, R. W., Reitman, N. G., Gold, R. D., & Hayes, G. P. (2015). Evidence for slip partitioning and bimodal slip behavior on a single fault: Surface slip characteristics of the 2013 Mw7.7 Balochistan, Pakistan earthquake. *Earth and Planetary Science Letters*, *420*, 1–11. https://doi.org/10.1016/j.epsl.2015.03.027

Barnhart, W. D., Hayes, G. P., & Gold, R. D. (2019). The July 2019 Ridgecrest, California earthquake sequence: Kinematics of slip and stressing in cross-fault ruptures. *Geophysical Research Letters*, *46*, 11859–11867. https://doi.org/10.1029/2019GL084741

Beanland, S., & Clark, M. M. (1994). *The Owens Valley fault zone, eastern California, and surface faulting associated with the 1872 earthquake (U.S. Geological survey Bulletin No. 1982)*. U.S. Geological Survey.

Behr, W. M., Rood, D. H., Fletcher, K. E., Guzman, N., Finkel, R., Hanks, T. C., et al. (2010). Uncertainties in slip-rate estimates for the Mission Creek strand of the southern San Andreas fault at Biskra Palms Oasis, southern California. *Geological Society of America Bulletin*, *122*, 1360–1377. https://doi.org/10.1130/B30020.1

Bell, J. W., Amelung, F., & Henry, C. D. (2012). InSAR analysis of the 2008 Reno-Mogul earthquake swarm: Evidence for westward migration of Walker Lane style dextral faulting. *Geophysical Research Letters*, *39*, L18306. https://doi.org/10.1029/2012GL052795

Bell, J. W., Caskey, S. J., Ramelli, A. R., & Guerrieri, L. (2004). Pattern and rates of faulting in the central Nevada seismic belt, and paleoseismic evidence for prior beltlike behavior. *Bulletin of the Seismological Society of America*, *94*, 1229–1254.

Bell, J. W., dePolo, C. M., Ramelli, A. R., Sarna-Wojcicki, A. M., & Meyer, C. E. (1999). Surface faulting and paleoseismic history of the 1932 Cedar Mountain earthquake area, west-central Nevada, and implications for modern tectonics of the Walker Lane. *Geological Society of America Bulletin*, *111*, 791–807. https://doi.org/10.1130/0016-7606(1999)111<0791:SFAPHO>2.3.CO;2

Bellier, O., & Zoback, M. L. (1995). Recent state of stress change in the Walker Lane zone, western Basin and Range province, United States. *Tectonics*, *14*, 564–593. https://doi.org/10.1029/94TC00596

Bennett, R. A., Wernicke, B. P., Niemi, N. A., Friedrich, A. M., & Davis, J. L. (2003). Contemporary strain rates in the northern Basin and Range province from GPS data. *Tectonics*, *22*, 31. https://doi.org/10.1029/2001TC001355

Birkeland, P. W. (1984). *Soils and geomorphology*. New York, NY: Oxford University Press.

Blard, P.-H., Lavé, J., Pik, R., Wagnon, P., & Bourlès, D. (2007). Persistence of full glacial conditions in the central Pacific until 15,000 years ago. *Nature*, *449*, 591–594. https://doi.org/10.1038/nature06142

Blewitt, G., Hammond, W. C., & Kreemer, C. (2018). Harnessing the GPS data explosion for interdisciplinary science. *Eos*, *99*. https://doi.org/10.1029/2018EO104623

Blewitt, G., Kreemer, C., Hammond, W. C., & Gazeaux, J. (2016). MIDAS robust trend estimator for accurate GPS station velocities without step detection. *Journal of Geophysical Research: Solid Earth*, *121*, 2054–2068. https://doi.org/10.1002/2015JB012552

Blewitt, G., Kreemer, C., Hammond, W. C., & Goldfarb, J. M. (2013). Terrestrial reference frame NA12 for crustal deformation studies in North America. *Journal of Geodynamics*, *72*, 11–24. https://doi.org/10.1016/j.jog.2013.08.004

Borchers, B., Marrero, S., Balco, G., Caffee, M., Goehring, B., Lifton, N., et al. (2016). Geological calibration of spallation production rates in the CRONUS-Earth project. *Quaternary Geochronology*, *31*, 188–198. https://doi.org/10.1016/j.quageo.2015.01.009

Bormann, J. M., Hammond, W. C., Kreemer, C., & Blewitt, G. (2016). Accommodation of missing shear strain in the Central Walker Lane, western North America: Constraints from dense GPS measurements. *Earth and Planetary Science Letters*, *440*, 169–177. https://doi.org/10.1016/j.epsl.2016.01.015

Bormann, J. M., Hammond, W. C., Kreemer, C., Blewitt, G., Jha, S. (2013). *A synoptic model of fault slip rates in the Eastern California Shear zone and Walker Lane from GPS velocities for seismic hazard studies*. Presented at the 2013 Seismological Society of America Annual Meeting, Seismological Research Letters, Salt Lake City, UT, p. 323.

Bormann, J. M., Surpless, B. E., Caffee, M. W., & Wesnousky, S. G. (2012). Holocene earthquakes and late Pleistocene slip-rate estimates on the Wassuk range fault zone, Nevada. *Bulletin of the Seismological Society of America*, *102*, 1884–1891. https://doi.org/10.1785/0120110287

Briggs, R. W. (2004). Late Pleistocene fault slip rate, earthquake recurrence, and recency of slip along the Pyramid Lake fault zone, northern Walker Lane, United States. *Journal of Geophysical Research*, *109*, B08402. https://doi.org/10.1029/2003JB002717

Briggs, R. W., & Wesnousky, S. G. (2005). Late Pleistocene and Holocene paleoearthquake activity of the Olinghouse fault zone, Nevada. *Bulletin of the Seismological Society of America*, *95*, 1301–1313. https://doi.org/10.1785/0120040129

Buer, N. J. V., Miller, E. L., & Dumitru, T. A. (2009). Early Tertiary paleogeologic map of the northern Sierra Nevada batholith and the northwestern Basin and Range. *Geology*, *37*, 371–374. https://doi.org/10.1130/G25448A.1

Bull, W. B. (1991). *Geomorphic Responses to Climatic Change*, (pp. 326). New York, NY: Oxford University Press.

Calzolari, G., Rossetti, F., Seta, M. D., Nozaem, R., Olivetti, V., Balestrieri, M. L., et al. (2016). Spatiotemporal evolution of intraplate strike-slip faulting: The Neogene–Quaternary Kuh-e-Faghan fault, central Iran. *GSA Bulletin*, *128*, 374–396. https://doi.org/10.1130/B31266.1

Carlson, C. (2017). *Kinematics and transfer mechanisms of strain accommodation at the transition between the Northern and Central Walker Lane, Western Nevada* (Doctoral Dissertation). Reno, NV: University of Nevada.

Cashman, P., Trexler, J., Muntean, T., Faulds, J., Louie, J., & Oppliger, G. (2009). Neogene tectonic evolution of the Sierra Nevada – Basin and range transition zone at the latitude of Carson city, Nevada. *Special Papers - Geological Society of America*, *447*. https://doi.org/10.1130/2009.2447(10)

Cashman, P. H., & Fontaine, S. A. (2000). Strain partitioning in the northern Walker Lane, western Nevada and northeastern California. *Tectonophysics*, *326*, 111–130.

Caskey, S. J. (1995). Geometric relations of dip slip to a faulted ground surface: New nomograms for estimating components of fault displacement. *Journal of Structural Geology*, *17*, 1197–1202. https://doi.org/10.1016/0191-8141(95)00023-7

Choi, N. H. (2016). *Late Pleistocene Slip Rate along the Panamint Valley Fault System, Eastern California (Masters Thesis)*, Oregon State University.

Chupik, C. (2019). Quaternary Mapping and Paleoseismic Assessment of the Warm Springs valley fault in the Northern Walker Lane, Nevada (Thesis). Reno, NV: University of Nevada.

dePolo, C. M., & Sawyer, T. (2005). *Paleoseismic studies along the eastern Carson Valley fault system* (Report no. USGS NEHRP 03HQGR0090). U.S. Geological Survey National Hazards Reduction Program.

Dixon, T. H., Miller, M., Farina, F., Wang, H., & Johnson, D. (2000). Present-day motion of the Sierra Nevada block and some tectonic implications for the Basin and Range province, North American Cordillera. *Tectonics*, *19*, 1–24.

Dohrenwend, J. C. (1982). *Surficial geologic Map of the Walker Lake 1 degree x 2 degrees quadrangle, Nevada- California. Miscellaneous Field Studies Map MF-1382-C.*

Dong, S., Ucarkus, G., Wesnousky, S. G., Maloney, J., Kent, G., Driscoll, N., & Baskin, R. (2014). Strike-slip faulting along the Wassuk range of the northern Walker Lane, Nevada. *Geosphere*, *10*, 40–48.

Dyksterhuis, S., & Müller, R. D. (2008). Cause and evolution of intraplate orogeny in Australia. *Geology*, *36*, 495–498. https://doi.org/10.1130/G24536A.1

Faulds, J. E., & Henry, C. D. (2008). Tectonic influences on the spatial and temporal evolution of the Walker Lane: An incipient transform fault along the evolving Pacific – North American plate boundary. In J. E. Spencer & S. R. Titley (Eds.), *Ores and orogenesis: Circum-Pacific tectonics, geologic evolution, and ore deposits* (*22*, pp. 437–470). Arizona Geological Society Digest.

Faulds, J. E., Henry, C. D., & Hinz, N. H. (2005). Kinematics of the northern Walker Lane: An incipient transform fault along the Pacific–North American plate boundary. *Geology*, *33*, 505–508.

Field, E. H., Jackson, D. D., & Dolan, J. F. (1999). A mutually consistent seismic-hazard source model for southern California. *Bulletin of the Seismological Society of America*, *89*, 559–578.

Frankel, K. L., Dolan, J. F., Finkel, R. C., Owen, L. A., & Hoeft, J. S. (2007). Spatial variations in slip rate along the Death Valley-Fish Lake Valley fault system determined from LiDAR topographic data and cosmogenic ^{10}Be geochronology. *Geophysical Research Letters*, *34*, L18303. https://doi.org/10.1029/2007GL030549

Frankel, K. L., Dolan, J. F., Owen, L. A., Ganev, P., & Finkel, R. C. (2011). Spatial and temporal constancy of seismic strain release along an evolving segment of the Pacific–North America plate boundary. *Earth and Planetary Science Letters*, *304*, 565–576. https://doi.org/10.1016/j.epsl.2011.02.034

Ganev, P. N., Dolan, J. F., Frankel, K. L., & Finkel, R. C. (2010). Rates of extension along the Fish Lake Valley fault and transtensional deformation in the Eastern California shear zone–Walker Lane belt. *Lithosphere*, *2*, 33–49. https://doi.org/10.1130/L51.1

Garvin, C. D., Hanks, T. C., Finkel, R. C., & Heimsath, A. M. (2005). Episodic incision of the Colorado River in Glen Canyon, Utah. *Earth Surface Processes and Landforms*, *30*, 973–984. https://doi.org/10.1002/esp.1257

Gilbert, C. M., & Reynolds, M. W. (1973). Character and chronology of basin development, western margin of the basin and range province. *Geological Society of America Bulletin*, *84*, 2489. https://doi.org/10.1130/0016-7606(1973)84<2489:CACOBD>2.0.CO;2

Gold, R., dePolo, C., Briggs, R., Crone, A., & Gosse, J. (2013). Late Quaternary slip-rate variations along the Warm Springs valley fault system, northern Walker Lane, California–Nevada Border. *Bulletin of the Seismological Society of America*, *103*, 542–558. https://doi.org/10.1785/0120120020

Gold, R. D., Briggs, R. W., Crone, A. J., & DuRoss, C. B. (2017). Refining fault slip rates using multiple displaced terrace risers – An example from the Honey Lake fault, NE California, USA. *Earth and Planetary Science Letters*, *477*, 134–146. https://doi.org/10.1016/j.epsl.2017.08.021

Gold, R. D., Briggs, R. W., Personius, S. F., Crone, A. J., Mahan, S. A., & Angster, S. J. (2014). Latest Quaternary paleoseismology and evidence of distributed dextral shear along the Mohawk Valley fault zone, northern Walker Lane, California: Paleoseismology Mohawk Valley fault zone. *Journal of Geophysical Research: Solid Earth*, *119*, 5014–5032. https://doi.org/10.1002/2014JB010987

Gold, R. D., Reitman, N. G., Briggs, R. W., Barnhart, W. D., Hayes, G. P., & Wilson, E. (2015). On- and off-fault deformation associated with the September 2013 Mw 7.7 Balochistan earthquake: Implications for geologic slip rate measurements. *Tectonophysics*, *660*, 65–78. https://doi.org/10.1016/j.tecto.2015.08.019

Gosse, J. C., & Phillips, F. M. (2001). Terrestrial in situ cosmogenic nuclides: Theory and application. *Quaternary Science Reviews*, *20*, 1475–1560.

Guest, B., Niemi, N., & Wernicke, B. (2007). Stateline fault system: A new component of the Miocene-Quaternary Eastern California shear zone. *GSA Bulletin*, *119*, 1337–1347. https://doi.org/10.1130/0016-7606(2007)119[1337:SFSANC]2.0.CO;2

Haddon, E. K., Amos, C. B., Zielke, O., Jayko, A. S., & Bürgmann, R. (2016). Surface slip during large Owens Valley earthquakes. *Geochemistry, Geophysics, Geosystems*, *17*, 2239–2269. https://doi.org/10.1002/2015GC006033

Hammond, W. C., Blewitt, G., & Kreemer, C. (2011). Block modeling of crustal deformation of the northern Walker Lane and Basin and Range from GPS velocities. *Journal of Geophysical Research*, *116*, B04402. https://doi.org/10.1029/2010JB007817

Hammond, W. C., Kreemer, C., & Blewitt, G. (2009). Geodetic constraints on contemporary deformation in the northern Walker Lane: 3. Central Nevada seismic belt postseismic relaxation. In J. S. Oldow & P. H. Cashman (Eds.), *Late Cenozoic structure and evolution of the Great Basin-Sierra Nevada Transition* (pp. 33–54). Special Papers of the Geological Society of America.

Hammond, W. C., Kreemer, C., Blewitt, G., & Plag, H.-P. (2010). Effect of viscoelastic postseismic relaxation on estimates of interseismic crustal strain accumulation at Yucca mountain, Nevada. *Geophysical Research Letters 37*, L06307. n/a-n/a. https://doi.org/10.1029/2010GL042795

Hammond, W. C., & Thatcher, W. (2005). Northwest Basin and range tectonic deformation observed with the global positioning system, 1999–2003. *Journal of Geophysical Research*, *110*, B10405. https://doi.org/10.1029/2005JB003678

Hammond, W. C., & Thatcher, W. (2007). Crustal deformation across the Sierra Nevada, northern Walker Lane, Basin and Range transition, western United States measured with GPS, 2000–2004. *Journal of Geophysical Research*, *112*, B05411. https://doi.org/10.1029/2006JB004625

Hatch, R., Smith, K., Abercrombie, R., Ruhl, C., Hammond, W., & Pierce, I. (2019). Relocations and tectonic implications of the Nine Mile Ranch sequence from 2016-2018: 3 Mw 5.4-5.6 near Hawthorne, Nevada. *Program with Abstracts. Presented at the Annual Meeting of the Seismological* (pp. 1069). Seattle, WA: Society of America, Seismological Research Letters.

Hatem, A. E., Cooke, M. L., & Toeneboehn, K. (2017). Strain localization and evolving kinematic efficiency of initiating strike-slip faults within wet kaolin experiments. *Journal of Structural Geology*, *101*, 96–108. https://doi.org/10.1016/j.jsg.2017.06.011

Herbert, J. W., Cooke, M. L., Oskin, M., & Difo, O. (2014). How much can off-fault deformation contribute to the slip rate discrepancy within the eastern California shear zone? *Geology*, *42*, 71–75. https://doi.org/10.1130/g34738.1

Hidy, A. J., Gosse, J. C., Pederson, J. L., Mattern, J. P., & Finkel, R. C. (2010). A geologically constrained Monte Carlo approach to modeling exposure ages from profiles of cosmogenic nuclides: An example from Lees Ferry, Arizona. *Geochemistry, Geophysics, Geosystems*, *11*, Q0AA10. https://doi.org/10.1029/2010GC003084

Hill, D. P., & Thatcher, W. (1992). An energy constraint for frictional slip on misoriented faults. *Bulletin of the Seismological Society of America*, *82*, 883–897.

Hunter, L. E., Howle, J. F., Rose, R. S., & Bawden, G. W. (2011). LiDAR-assisted identification of an active fault near Truckee, California. *Bulletin of the Seismological Society of America*, *101*, 1162–1181. https://doi.org/10.1785/0120090261

Jobe, J. A. T., Philibosian, B., Chupik, C., Dawson, T., Bennett, S. E. K., Gold, R., et al. (2020). Evidence of previous faulting along the 2019 Ridgecrest, California, earthquake ruptures. *Bulletin of the Seismological Society of America*, *110*. https://doi.org/10.1785/0120200041

Kent, G. M., Babcock, J. M., Driscoll, N. W., Harding, A. J., Dingler, J. A., Seitz, G. G., et al. (2005). 60 k.y. record of extension across the western boundary of the Basin and Range province: Estimate of slip rates from offset shoreline terraces and a catastrophic slide beneath Lake Tahoe. *Geology*, *33*, 365–368. https://doi.org/10.1130/G21230.1

Kirby, E., Anandakrishnan, S., Phillips, F., & Marrero, S. (2008). Late Pleistocene slip rate along the Owens Valley fault, eastern California. *Geophysical Research Letters*, *35*, L01304. https://doi.org/10.1029/2007GL031970

Kirby, E., Burbank, D. W., Reheis, M., & Phillips, F. (2006). Temporal variations in slip rate of the white mountain fault zone, eastern California. *Earth and Planetary Science Letters*, *248*, 168–185. https://doi.org/10.1016/j.epsl.2006.05.026

Koehler, R. D., Dee, S., Elliott, A., Hatem, A. E., Pickering, A., Pierce, I., & Seitz, G. (2021). In review field response and surface rupture characteristics of the 2020 Mw6.5 Monte Cristo Range earthquake, central Walker Lane, Nevada. *Seismological Research Letters*. https://doi.org/10.1785/0220200371

Koehler, R. D., & Wesnousky, S. G. (2011). Late Pleistocene regional extension rate derived from earthquake geology of late Quaternary faults across the Great Basin, Nevada, between 38.5° N and 40° N latitude. *The Geological Society of America Bulletin*, *123*, 631–650.

Kohl, C. P., & Nishiizumi, K. (1992). Chemical isolation of quartz for measurement of in-situ-produced cosmogenic nuclides. *Geochimica et Cosmochimica Acta*, *56*, 3583–3587.

Lal, D. (1991). Cosmic ray labeling of erosion surfaces: In situ nuclide production rates and erosion models. *Earth and Planetary Science Letters*, *104*, 424–439.

Lamb, S., Arnold, R., & Moore, J. D. P. (2018). Locking on a megathrust as a cause of distributed faulting and fault-jumping earthquakes. *Nature Geoscience*, *11*, 871–875. https://doi.org/10.1038/s41561-018-0230-5

Lee, J., Spencer, J., & Owen, L. (2001). Holocene slip rates along the Owens Valley fault, California: Implications for the recent evolution of the eastern California shear zone. *Geology*, *29*, 819–822. https://doi.org/10.1130/0091-7613(2001)029<0819:HSRATO>2.0.CO;2

Li, X., Huang, W., Pierce, I. K. D., Angster, S. J., & Wesnousky, S. G. (2017). Characterizing the Quaternary expression of active faulting along the Olinghouse, Carson, and Wabuska lineaments of the Walker Lane. *Geosphere*, *13*, 2119–2136. https://doi.org/10.1130/GES01483.1

Lifton, N. (2016). Implications of two Holocene time-dependent geomagnetic models for cosmogenic nuclide production rate scaling. *Earth and Planetary Science Letters*, *433*, 257–268. https://doi.org/10.1016/j.epsl.2015.11.006

Lifton, N., Sato, T., & Dunai, T. J. (2014). Scaling in situ cosmogenic nuclide production rates using analytical approximations to atmospheric cosmic-ray fluxes. *Earth and Planetary Science Letters*, *386*, 149–160. https://doi.org/10.1016/j.epsl.2013.10.052

Lifton, Z. M., Newman, A. V., Frankel, K. L., Johnson, C. W., & Dixon, T. H. (2013). Insights into distributed plate rates across the Walker Lane from GPS geodesy: Walker Lane GPS. *Geophysical Research Letters*, *40*, 4620–4624. https://doi.org/10.1002/grl.50804

Link, M. H., Roberts, M. T., & Newton, M. S. (1985). Walker Lake basin, Nevada: An example of Late Tertiary (?) to recent sedimentation in a basin adjacent to an active strike-slip fault. In T. B. Kevin, & C-B. Nicholas (Eds.) *Strike-slip deformation, basin formation, and sedimentation*. Society for Sedimentary Geology.

Long, S. P. (2019). Geometry and magnitude of extension in the Basin and Range Province (39°N), Utah, Nevada, and California, USA: Constraints from a province-scale cross section. *GSA Bulletin*, *131*, 99–119. https://doi.org/10.1130/B31974.1

Maloney, J. M., Noble, P. J., Driscoll, N. W., Kent, G. M., Smith, S. B., Schmauder, G. C., et al. (2013). Paleoseismic history of the fallen leaf segment of the west Tahoe-Dollar point fault reconstructed from slide deposits in the Lake Tahoe basin, California-Nevada. *Geosphere*, *9*, 1065–1090. https://doi.org/10.1130/GES00877.1

Mann, P. (2007). Global catalogue, classification and tectonic origins of restraining- and releasing bends on active and ancient strike-slip fault systems. *Geological Society London Special Publications*, *290*, 13–142. https://doi.org/10.1144/SP290.2

Martin, L. C. P., Blard, P.-H., Balco, G., Lavé, J., Delunel, R., Lifton, N., & Laurent, V. (2017). The CREp program and the ICE-D production rate calibration database: A fully parameterizable and updated online tool to compute cosmic-ray exposure ages. *Quaternary Geochronology*, *38*, 25–49. https://doi.org/10.1016/j.quageo.2016.11.006

Matenco, L., Bertotti, G., Leever, K., Cloetingh, S., Schmid, S. M., Tărăpoancă, M., & Dinu, C. (2007). Large-scale deformation in a locked collisional boundary: Interplay between subsidence and uplift, intraplate stress, and inherited lithospheric structure in the late stage of the SE Carpathians evolution. *Tectonics*, *26*, TC4011. https://doi.org/10.1029/2006TC001951

McCalpin, J. (2009). *Paleoseismology* (2nd ed.). Academic Press.

Milliner, C. W. D., Dolan, J. F., Hollingsworth, J., Leprince, S., Ayoub, F., & Sammis, C. G. (2015). Quantifying near-field and off-fault deformation patterns of the 1992 Mw 7.3 Landers earthquake. *Geochemistry, Geophysics, Geosystems*, *16*(5), 1577–1598. https://doi.org/10.1002/2014GC005693

Molnar, P. (1988). Continental tectonics in the aftermath of plate tectonics. *Nature*, *335*, 131. https://doi.org/10.1038/335131a0

Nagorsen-Rinke, S., Lee, J., & Calvert, A. (2013). Pliocene sinistral slip across the Adobe Hills, eastern California-western Nevada: Kinematics of fault slip transfer across the Mina deflection. *Geosphere*, *9*, 37–53.

Nishiizumi, K., Winterer, E. L., Kohl, C. P., Klein, J., Middleton, R., Lal, D., & Arnold, J. R. (1989). Cosmic ray production rates of ^{10}Be and ^{26}Al in quartz from glacially polished rocks. *Journal of Geophysical Research*, *94*, 17907–17915. https://doi.org/10.1029/JB094iB12p17907

Olive, J.-A., & Behn, M. D. (2014). Rapid rotation of normal faults due to flexural stresses: An explanation for the global distribution of normal fault dips. *Journal of Geophysical Research: Solid Earth*, *119*, 3722–3739. https://doi.org/10.1002/2013JB010512

Oskin, M. E., Arrowsmith, J. R., Corona, A. H., Elliott, A. J., Fletcher, J. M., Fielding, E. J., et al. (2012). Near-field deformation from the El Mayor–Cucapah earthquake revealed by differential LIDAR. *Science*, *335*, 702–705. https://doi.org/10.1126/science.1213778

Owen, L. A., Frankel, K. L., Knott, J. R., Reynhout, S., Finkel, R. C., Dolan, J. F., & Lee, J. (2011). Beryllium-10 terrestrial cosmogenic nuclide surface exposure dating of Quaternary landforms in Death Valley. *Geomorphology*, *125*, 541–557. https://doi.org/10.1016/j.geomorph.2010.10.024

Pardo, C. D., Smith-Konter, B. R., Serpa, L. F., Kreemer, C., Blewitt, G., & Hammond, W. C. (2012). Interseismic deformation and geologic evolution of the Death Valley fault zone. *Journal of Geophysical Research*, *117*, B06404. https://doi.org/10.1029/2011JB008552

Personius, S. F., Briggs, R. W., Maharrey, J. Z., Angster, S. J., & Mahan, S. A. (2017). A paleoseismic transect across the northwestern Basin and Range Province, northwestern Nevada and northeastern California, USA. *Geosphere*, *13*, 782–810. https://doi.org/10.1130/GES01380.1

Petersen, M., Zeng, Y., Haller, K., McCaffrey, R., Hammond, W., Bird, P., et al. (2014). Geodesy- and geology-based slip-rate models for the western United States (excluding California) National seismic hazard maps. *Geol. Fac. Publ. Present.*, *80*. https://doi.org/10.3133/ofr20131293

Petronis, M. S., Geissman, J. W., Oldow, J. S., & McIntosh, W. C. (2009). Late Miocene to Pliocene vertical-axis rotation attending development of the Silver Peak–Lone Mountain displacement transfer zone, west-central Nevada. In S. O. John, & H. C. Patricia (Eds.), *Late Cenozoic structure and evolution of the Great Basin-Sierra Nevada Transition*, (pp. 215–254). Geological Society of America. https://doi.org/10.1130/2009.2447(12)

Phillips, F. M., Zreda, M., Smith, S. S., Elmore, D., Kubik, P. W., & Sharma, P. (1990). Cosmogenic Chlorine-36 chronology for glacial deposits at Bloody Canyon, eastern Sierra Nevada. *Science*, *248*, 1529–1532.

Pierce, I. K. D., Wesnousky, S. G., & Owen, L. A. (2017). Terrestrial cosmogenic surface exposure dating of moraines at Lake Tahoe in the Sierra Nevada of California and slip rate estimate for the West Tahoe Fault. *Geomorphology*, *298*, 63–71. https://doi.org/10.1016/j.geomorph.2017.09.030

Pierce, I. K. D., Wesnousky, S., Owen, L., Bormann, J. M., Li, X., & Caffee, M. W. (2021). Walker Lane GPS Rates. PANGAEA. https://doi.org/10.1594/PANGAEA.926828

Raimondo, T., Hand, M., & Collins, W. J. (2014). Compressional intracontinental orogens: Ancient and modern perspectives. *Earth-Science Reviews*, *130*, 128–153. https://doi.org/10.1016/j.earscirev.2013.11.009

Ramelli, A. R., Bell, J. W., dePolo, C. M., & Yount, J. C. (1999). Large-magnitude, late Holocene earthquakes on the Genoa fault, west-central Nevada and eastern California. *Bulletin of the Seismological Society of America*, *89*, 1458–1472.

Reheis, M. (1999). *Extent of Pleistocene lakes in the western Great Basin. Miscellaneous Field Studies*.

Richardson, C. A., & Seedorff, E. (2017). Estimating friction in normal fault systems of the Basin and Range province and examining its geological context. *Geological Society London Special Publications*, *458*, 155–179. https://doi.org/10.1144/SP458.8

Riguzzi, F., Crespi, M., Devoti, R., Doglioni, C., Pietrantonio, G., & Pisani, A. R. (2012). Geodetic strain rate and earthquake size: New clues for seismic hazard studies. *Physics of the Earth and Planetary Interiors*, *206–207*, 67–75. https://doi.org/10.1016/j.pepi.2012.07.005

Rockwell, T. K. (2000). Paleoseismology of the Johnson valley, Kickapoo, and Homestead valley faults: Clustering of earthquakes in the eastern California shear zone. *Bulletin of the Seismological Society of America*, *90*, 1200–1236. https://doi.org/10.1785/0119990023

Rollins, C., & Avouac, J.-P. (2019). A geodesy- and seismicity-based local earthquake likelihood model for central Los Angeles. *Geophysical Research Letters*, *46*, 3153–3162. https://doi.org/10.1029/2018GL080868

Rood, D. H., Burbank, D. W., & Finkel, R. C. (2011). Spatiotemporal patterns of fault slip rates across the Central Sierra Nevada frontal fault zone. *Earth and Planetary Science Letters*, *301*, 457–468. https://doi.org/10.1016/j.epsl.2010.11.006

Rubin, C. M., & Sieh, K. (1997). Long dormancy, low slip rate, and similar slip-per-event for the Emerson fault, eastern California shear zone. *Journal of Geophysical Research*, *102*, 15319–15333. https://doi.org/10.1029/97JB00265

Ruhl, C., Abercrombie, R., Smith, K., & Zaliapin, I. (2016). Complex spatiotemporal evolution of the 2008 Mw 4.9 Mogul earthquake swarm (Reno, Nevada): Interplay of Fluid and faulting. *Journal of Geophysical Research: Solid Earth*, *121*, 8196–8216. https://doi.org/10.1002/2016JB013399

Sarmiento, A. C., Wesnousky, S. G., & Bormann, J. M. (2011). Paleoseismic Trenches across the Sierra Nevada and Carson Range Fronts in Antelope Valley, California, and Reno, Nevada. *Bulletin of the Seismological Society of America*, *101*, 2542–2549. https://doi.org/10.1785/0120100176

Scholz, C. (2019). *The mechanics of earthquakes and faulting* (3rd ed.). Cambridge, UK: Cambridge University Press.

Schreurs, G. (2003). Fault development and interaction in distributed strike-slip shear zones: An experimental approach. *Geological Society London Special Publications*, *210*, 35–52. https://doi.org/10.1144/GSL.SP.2003.210.01.03

Sibson, R. H. (1985). A note on fault reactivation. *Journal of Structural Geology*, *7*, 751–754. https://doi.org/10.1016/0191-8141(85)90150-6

Stauffer, H. (2003). *Timing of the Last Highstand of Pluvial Lake Wellington, Smith Valley, Nevada (Master's Thesis)*, San Jose State University.

Stewart, J. H. (1988). Tectonics of the Walker Lane belt, western Great Basin Mesozoic and Cenozoic deformation in a zone of shear. In W. G. Ernst (Ed.), *Metamophism and crustal evolution of the Western US* (pp. 685–713). Englewood Cliffs, NJ: Prentice Hall.

Stirling, M. W., Wesnousky, S. G., & Shimazaki, K. (1996). Fault trace complexity, cumulative slip, and the shape of the magnitude-frequency distribution for strike-slip faults: A global survey. *Geophysical Journal International*, *124*, 833–868. https://doi.org/10.1111/j.1365-246X.1996.tb05641.x

Stockli, D. F., Dumitru, T. A., McWilliams, M. O., & Farley, K. A. (2003). Cenozoic tectonic evolution of the white mountains, California and Nevada. *The Geological Society of America Bulletin*, *115*, 788–816.

Stone, J. O. (2000). Air pressure and cosmogenic isotope production. *Journal of Geophysical Research*, *105*, 23753–23759.

Styron, R. (2019). The impact of earthquake cycle variability on neotectonic and paleoseismic slip rate estimates. *Solid Earth*, *10*, 15–25. https://doi.org/10.5194/se-10-15-2019

Surpless, B., & Kroeger, G. (2015). The unusual temporal and spatial slip history of the Wassuk Range normal fault, western Nevada (USA): Implications for seismic hazard and Walker Lane deformation. *The Geological Society of America Bulletin*, *127*, 737–758. https://doi.org/10.1130/B31159.1

Surpless, B. E., Stockli, D. F., Dumitru, T. A., & Miller, E. L. (2002). Two-phase westward encroachment of Basin and Range extension into the northern Sierra Nevada. *Tectonics*, *21*, 2-1–2-10. https://doi.org/10.1029/2000tc001257

Sylvester, A. G. (1988). Strike-slip faults. *GSA Bulletin*, *100*, 1666–1703. https://doi.org/10.1130/0016-7606(1988)100<1666:SSF>2.3.CO;2

Thatcher, W., Foulger, G. R., Julian, B. R., Svarc, J., Quilty, E., & Bawden, G. W. (1999). Present-day deformation across the basin and range province, western United States. *Science*, *283*, 1714–1717.

Thatcher, W., & Hill, D. P. (1991). Fault orientations in extensional and conjugate strike-slip environments and their implications. *Geology*, *19*, 1116–1120. https://doi.org/10.1130/0091-7613(1991)019<1116:FOIEAC>2.3.CO;2

Unruh, J., Humphrey, J., & Barron, A. (2003). Transtensional model for the Sierra Nevada frontal fault system, eastern California. *Geology*, *31*, 327–330.

Uppala, S. M., Kallberg, P. W., Simmons, A. J., Andrae, U., Bechtold, V. D. C., Fiorino, M., et al. (2005). The ERA-40 re-analysis. *Quarterly Journal of the Royal Meteorological Society*, *131*, 2961–3012. https://doi.org/10.1256/qj.04.176

USGS. (2020). *U.S. Geological Survey Quaternary fault and fold database for the United States*.

Wesnousky, S. G. (1988). Seismological and structural evolution of strike-slip faults. *Nature*, *335*, 340. https://doi.org/10.1038/335340a0

Wesnousky, S. G. (2005). Active faulting in the Walker Lane. *Tectonics*, *24*, 35. https://doi.org/10.1029/2004TC001645

Wesnousky, S. G. (2008). Displacement and geometrical characteristics of earthquake surface ruptures: Issues and implications for seismic-hazard analysis and the process of earthquake rupture. *Bulletin of the Seismological Society of America*, *98*, 1609–1632. https://doi.org/10.1785/0120070111

Wesnousky, S. G., Bormann, J. M., Kreemer, C., Hammond, W. C., & Brune, J. N. (2012). Neotectonics, geodesy, and seismic hazard in the northern Walker Lane of western North America: Thirty kilometers of crustal shear and no strike-slip? *Earth Planetary Science Letters*, *329–330*, 133–140. https://doi.org/10.1016/j.epsl.2012.02.018

Wesnousky, S. G., & Caffee, M. (2011). Range-bounding normal fault of Smith Valley, Nevada: Limits on age of Last surface-rupture earthquake and late Pleistocene rate of displacement. *Bulletin of the Seismological Society of America*, *101*, 1431–1437. https://doi.org/10.1785/0120100238

Wilcox, R. E., Harding, T. P., & Seely, D. R. (1973). Basic wrench tectonics. *AAPG Bulletin*, *57*, 74–96.

Zechar, J. D., & Frankel, K. L. (2009). Incorporating and reporting uncertainties in fault slip rates. *Journal of Geophysical Research*, *114*, B12407. https://doi.org/10.1029/2009JB006325

Ziegler, P. A., van Wees, J.-D., & Cloetingh, S. (1998). Mechanical controls on collision-related compressional intraplate deformation. *Tectonophysics*, *300*, 103–129. https://doi.org/10.1016/S0040-1951(98)00236-4

Zinke, R., Dolan, J. F., Dissen, R. V., Grenader, J. R., Rhodes, E. J., McGuire, C. P., et al. (2015). Evolution and progressive geomorphic manifestation of surface faulting: A comparison of the Wairau and Awatere faults, south Island, New Zealand. *Geology*, *43*, 1019–1022. https://doi.org/10.1130/G37065.1

Zuza, A. V., Yin, A., Lin, J., & Sun, M. (2017). Spacing and strength of active continental strike-slip faults. *Earth and Planetary Science Letters*, *457*, 49–62. https://doi.org/10.1016/j.epsl.2016.09.041

Reference From the Supporting Information

Shumway, A. M. (2019). *Data Release for the 2014 National Seismic Hazard Model for the Conterminous U.S.* United States Geological Survey. https://doi.org/10.5066/P9P77LGZ